Zircon growth in (U)HP quartzo-feldspathic host gneisses exhumed in the Woodlark Rift of Papua New Guinea

N. A. Zirakparvar[1,2], S. L. Baldwin[1], and A. K. Schmitt[3]

[1]Department of Earth Sciences, Syracuse University, Syracuse, New York, , USA, [2]Present address: Department of Earth and Planetary Sciences, American Museum of Natural History, Central Park West 79 St., New York, New York , 10024,, USA, [3]Department of Earth and Space Sciences, University of California, Los Angeles, California, , USA

Abstract To understand zircon behavior as a function of bulk composition and metamorphic grade in the world's youngest (U)HP terrane, we report U-Pb SIMS spot-mode and depth-profiling analyses for quartzo-feldspathic gneisses. Zircons from two gneisses contain Cretaceous inherited cores, with μm sized metamorphic rims requiring depth profiling for reliable dating. Linear regression of the common-Pb uncorrected data for rims yield $^{206}Pb/^{238}U$ ages of 2.89 $\pm$ 0.29 Ma and 2.77 $\pm$ 0.99 Ma (concordia intercept ages at 95% confidence). The older age is within two-sigma error of previously reported $^{206}Pb/^{238}U$ ages on zircons from mafic eclogite within the gneiss, indicating that rims formed on inherited cores within host gneisses during eclogite facies metamorphism. At the (U)HP locality zircons from host gneiss lack inheritance and yield a $^{206}Pb/^{238}U$ age of 3.66 $\pm$ 0.13 Ma. These results are younger than previously reported $^{206}Pb/^{238}U$ ages on zircons from coesite eclogite within the gneiss, but are within error of the youngest reported LA-ICP-MS $^{206}Pb/^{238}U$ zircon ages on retrogressed mafic eclogite. We also report intragrain geochemical heterogeneity, indicated by zircon Hf, Y, and Ti variations in depth profiles which suggest chemical disequilibrium over the interval of zircon growth. Collectively, these results indicate that zircon recrystallization and new growth of zircon rims on relict grains occurred during eclogite facies metamorphism and during subsequent retrogression, but not at (U)HP conditions. Comparison between results from PNG and other (U)HP terranes bolsters previous suggestions that the PNG (U)HP terrane evolved rapidly.

1. Introduction

Ultrahigh-pressure ((U)HP) metamorphic terranes comprise complex assemblages of highly deformed mafic and quartzo-feldspathic rocks. The P-T-t evolution of quartzo-feldspathic host gneiss relative to enclosed mafic eclogite is often poorly understood because diagnostic major (e.g., omphacite and almandine-pyrope garnet) or trace (e.g., coesite or microdiamond) (U)HP mineral assemblages are often absent, or not preserved in quartzo-feldspathic host gneisses. In both active and ancient tectonic settings, understanding the evolutionary paths of mafic eclogites and felsic host gneisses is a crucial piece of information in modeling the (U)HP terrane's rheologic properties at depth [e.g., *Brownlee et al.*, 2011], which in turn has implications for interpreting geophysical data and developing geodynamic models. Whether host gneisses were metamorphosed simultaneously with mafic eclogite can be addressed by combining geochronologic and trace element data [e.g., *Liati*, 2005]. For this purpose, zircon has been used extensively because it can form entirely new crystals or grow as rims on preexisting grains during metamorphism [*Rubatto et al.*, 1998; *Liati*, 2005; *McClelland et al.*, 2009; *Gao et al.*, 2011; *McClelland and Lapen*, 2013], and trace element systematics in zircons can be interpreted with respect to mineral reactions that change the bulk distribution coefficients during zircon growth [*Rubatto*, 2002; *Hanchar and VanWestrenen*, 2007; *Harley et al.*, 2007; *Harley and Kelly*, 2007; *Rubatto and Hermann*, 2007; *Scherer et al.*, 2007; *Monteleone et al.*, 2007]. However, the fact that zircon forms under a wide range of P-T conditions in silica-rich rocks also lends complexity to the interpretation of U-Pb zircon ages during mineral paragenesis in (U)HP quartzo-feldspathic gneisses.

The purpose of this study is to examine the U-Pb age and trace element distributions in zircons from three quartzo-feldspathic gneisses (Figure 1) in the (U)HP terrane exhumed in the western Woodlark Rift of Papua New Guinea (PNG). In this rapidly evolving plate boundary zone, extensional gneiss domes have exposed the world's youngest known (U)HP rocks and research has focused on understanding the geologic history
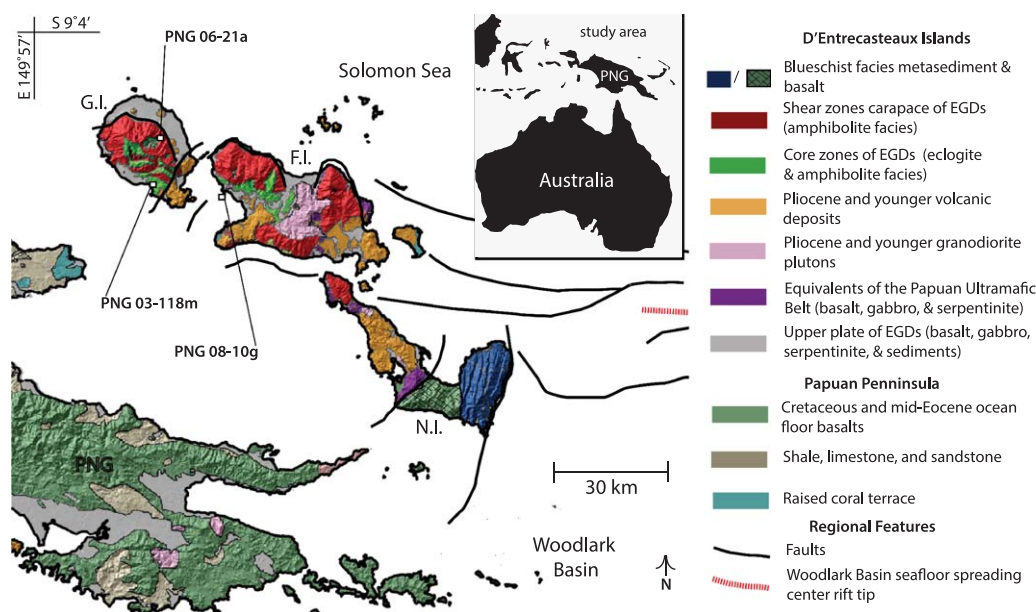
Figure 1. Geologic map of D'Entrecasteaux Islands region with sample localities and showing major lithological [*Monteleone et al.*, 2007; *Baldwin et al.*, 2008; *Davies*, 2012], structural [*Little et al.*, 2007], and topographic features [*Miller et al.*, 2012] of the region. Abbreviations are as follows: PNG = Papua New Guinea; G.I. = Goodenough Island; F.I. = Fergusson Island; N.I. = Normanby Island.

of this region at scales ranging from the entire Australia-Pacific (AUS-PAC) plate boundary down to the multistage evolution of individual minerals [*Baldwin et al.*, 1993, 2004, 2008; *Taylor et al.*, 1995; *Monteleone et al.*, 2001, 2007; *Little et al.*, 2011; *Zirakparvar et al.*, 2011, 2012; *Gordon et al.*, 2012]. This pre-existing body of research provides a framework within which to interpret the U-Pb age and trace element results from zircons in quartzo-feldspathic host gneisses, thereby allowing us to relate the observed U-Pb age and trace element data to specific processes in the tectonic evolution of the PNG (U)HP terrane.

Zircons in two samples from the Woodlark Rift exhibit internal morphologies, as revealed by cathode-Ray Luminescence (CL) imaging of polished zircon cross sections, consistent with an interpretation of older cores overgrown by younger rims (Figure 2). The rims are typically <5 μm thick, necessitating a sampling and analysis strategy with sufficient spatial resolution to fully resolve the U-Pb age and trace element systematics at the micron scale. In this study, Secondary Ionization Mass Spectrometry (SIMS) was used in spot mode to acquire U-Pb age data from polished zircon cross sections (Figure 3a). In addition, unpolished external crystal surfaces (Figure 3b) were analyzed via depth profiling [*Breeding et al.*, 2004; *Trail et al.*, 2007; *Gordon et al.*, 2009a, 2009b; *Zou et al.*, 2010; *Schneider et al.*, 2011] at variable depths (up to 15 μm) to
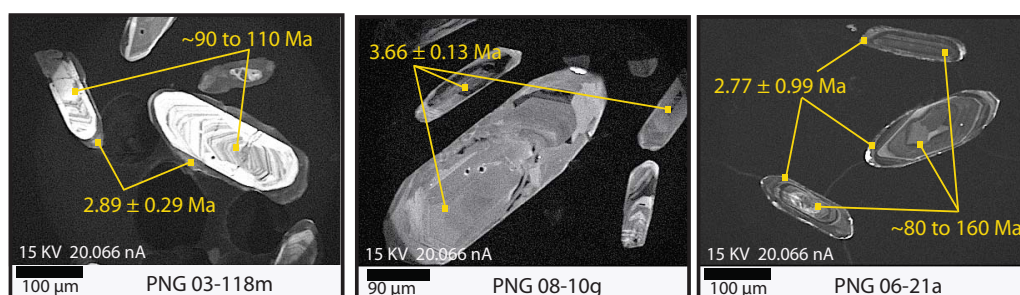
Figure 2. Selected cathode-ray luminescence (CL) images for zircons extracted from gneisses in the D'Entrecasteaux Islands. Note the up to 5 μm thick dark CL overgrowths for zircons from sample PNG 03-118m. Zircons from sample PNG 06-21a also exhibit dark CL overgrowths, although they are much thinner than in sample 03-118m and not visible in this image. Zircons from sample PNG 08-10g do not exhibit any dark CL overgrowths. See text for discussion of ages for zircons from these samples.
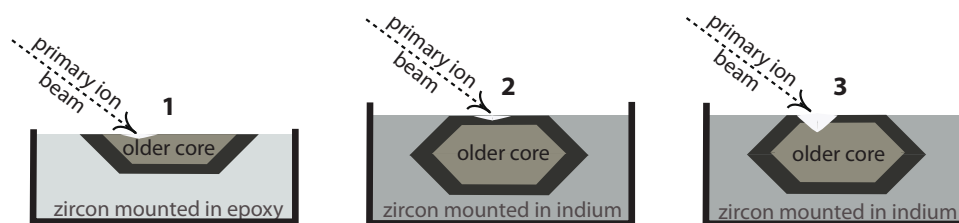
Figure 3. Schematic diagram illustrating different types of SIMS analyses ((1) spot mode for polished cross sections, (2) spot mode for unpolished external surface, and (3) depth profiling) performed in this study.

acquire U-Pb age and Ti, Hf, and Y concentration data at the submicron-scale resolution afforded by this technique (Figure 3c).

A comparison of the SIMS data acquired in this study with preexisting geochronology allows for an examination of the history of the quartzo-feldspathic gneisses relative to the prograde, peak (U)HP, and retrograde metamorphism as recorded by zircon U-Pb systematics. The SIMS depth-profiling results also provide unique insights into the spatial scale of trace element heterogeneity during zircon crystallization in a former subduction complex that is now being rifted apart. Lastly, the data acquired in this study facilitate detailed comparisons between the time scales of zircon crystallization in the PNG (U)HP metamorphic terrane and those reported from other (U)HP terranes globally [e.g., *McClelland and Lapen*, 2013].

2. Geologic Background and Samples Analyzed

2.1. Geologic Overview

Three quartzo-feldspathic gneiss samples were chosen for detailed SIMS analysis in this study. Samples were collected from extensional gneiss domes [*Hill*, 1994; *Little et al.*, 2007, 2011] in the D'Entrecasteaux Islands, southeastern PNG (Figure 1), which occur in a zone of active extension (i.e., Woodlark Rift) at the western apex of the Woodlark Basin. Samples are described in detail in section 2.2, whereas this section provides a general geologic overview of the region. Westward propagating seafloor spreading in the Woodlark Basin has occurred since ∼6 Ma [*Taylor et al.*, 1995], and the active seafloor-spreading rift tip is currently situated offshore northeast Normanby Island (Figure 1).

In the D'Entrecasteaux Islands, Cretaceous aged volcaniclastic sediments and basalts derived from the Gondwana rifted margin [*Zirakparvar et al.*, 2012] were subducted, metamorphosed at (U)HP conditions in the Late Miocene to Pliocene [*Monteleone et al.*, 2007; *Baldwin et al.*, 2008; *Zirakparvar et al.*, 2011], and since then have been exhumed to the surface during rifting [*Little et al.*, 2007, 2011; *Martinez et al.*, 2001; *Webb et al.*, 2008]. Remnants of subducted lithosphere are found in the core zones and shear zone carapaces of the D'Entrcasteaux Islands domes, where felsic and intermediate gneisses encapsulate mafic eclogites with Late Miocene–Pliocene metamorphic crystallization ages. U-Pb zircon and Lu-Hf garnet dating of the mafic eclogites [*Baldwin et al.*, 2004; *Monteleone et al.*, 2007; *Zirakparvar et al.*, 2011; *Gordon et al.*, 2012], and P-T constraints [*Davies and Warren*, 1992; *Hill and Baldwin*, 1993; *Baldwin et al.*, 2008], indicate that coesite eclogite in the D'Entrecasteaux Islands was exhumed from depths of at least 90 km since ∼8 Ma. K/Ar, $^{40}Ar/^{39}Ar$, and fission-track dating techniques applied to the lower-plate rocks have also documented extremely rapid (e.g., ≥100°C/Myr) cooling [*Baldwin et al.*, 1993]. It is not yet known when these rocks were subducted, but it is noteworthy that a large garnet porphyroblast in the shear zone carapace on Goodenough Island yielded a 68 ± 3.6 Ma Lu-Hf age [*Zirakparvar et al.*, 2011] coinciding with the timing of ophiolite obduction on the Papuan peninsula [*Lus et al.*, 2004] and the age of diabase drilled on Ocean Drilling Program (ODP) Leg 180 from the Moresby Seamount [*Monteleone et al.*, 2001]. In the D'Entrecasteaux Islands, seismic data [*Abers et al.*, 2002], stream profile analysis [*Miller et al.*, 2012], and thermochronologic data [*Baldwin et al.*, 1993], all suggest that exhumation of lower-plate rocks occurred during Plio-Pleistocene to Holocene time and may still be ongoing.

2.2. Samples Analyzed

Two of the quartzo-feldspathic gneiss samples (PNG 03-118m and PNG 08-10g; Figure 1) are core zone rocks hosting Miocene–Pliocene mafic eclogites, whereas a third sample (PNG 06-21a; Figure 1) is from

Table 1. Coordinates and published P-T-t constraints for samples analyzed in this study[a]

PNG 03-118m	
S 9° 29.167′	*For mafic eclogite boudin within sample PNG 03-118m*
E 150° 14.750′ Felsic host gneiss:	[b]Zircon $^{206}Pb/^{238}U$ age via SIMS = 2.09 ± 0.49 Ma interpreted as crystallization at eclogite or amphibolite conditions.
Qtz + Pl + Ms + Am	Zr in Rt therm = 677 to 817°C; Jd barom = min P of 14 kbar.
PNG 08-10g	
S 9° 29.319′	*For coesite eclogite boudin within sample PNG 08-010g*
E 150° 27.696′ Felsic host gneiss at	[b]Zircon $^{206}Pb/^{238}U$ age via SIMS = 7.9 ± 1.9 Ma and [c]Lu-Hf garnet age = 7.1 ± 0.7 Ma; both interpreted as recording
coesite locality: Qtz + Pl + Ms +Bt	crystallization at (U)HP conditions. [b]Zr in Rt therm. = 650–680°C;
	Jd barom. = min P of 15 kbar. [d]Amphibole from retrogressed rind $^{40}Ar/^{39}Ar$ age = 9.83 Ma.
	Muscovite from dike at same outcrop $^{40}Ar/^{39}Ar$ age = 3.52 ± 0.10 Ma.
	U-Pb results for mafic eclogite boudin without documented coesite
	[e]Zircon $^{206}Pb/^{238}U$ ages via LA-ICP-MS = 9.1 ± 0.6 Ma to 3.8 ± 1.0 Ma in retrogressed rim of
	eclogite, 7.4 ± 1.1 Ma to 4.1 ± 1.3 Ma in unretrogressed interior. Zircon $^{206}Pb/^{238}U$ ages
	via CA-TIMS = 5.82 ± 0.02 Ma to 4.78 ± 0.17 Ma.
PNG 06-21a	
S 9° 18.831′	*For rocks in same shear zone as sample PNG 06-21a*
E 150° 17.430′	$^{40}Ar/^{39}Ar$ ages for minerals in nearby samples from Wakonai shear zone: [d]muscovite = 1.5 Ma,
Shear zone gneiss:	biotite = 1.4 Ma, K-feldspar = 1.4 Ma.
Qtz + Pl + Ms + Grt + Chl	Apatite fission track for rocks in Wakonai shear zone = 0.8 Ma. [c]Sample <5 km away in
	Wakonai shear zone records garnet growth at 68 ± 3.6 Ma.

[a]The precise location and mineralogy of the three samples examined in this study is also provided. Mineral, and other, abbreviations are as follows: Qtz = quartz, Pl = plagioclase feldspar, Ms = muscovite, Am = amphibole, Bt = biotite, Grt = garnet, Zrn = zircon, Chl = chlorite, Kfs = K-feldspar, Zr = zirconium, Rt = rutile, Jd = jadeite.
Sources of data are as follows:
[b]Monteleone et al. [2007]; [c]Baldwin et al. [1993]; [d]Zirakparvar et al. [2011a]; [e]Gordon et al. [2012].

the Wakonai extensional shear zone carapace separating core zone rocks from the unmetamorphosed upper plate on northern Goodenough Island [*Baldwin et al.*, 1993; *Hill*, 1994; *Little et al.*, 2011]. Published data provide a framework within which to interpret the SIMS zircon U-Pb and trace element data acquired in this study. These preexisting constraints are summarized here and in Table 1.

2.2.1. Gneissic Host of ~2 Ma Eclogite: PNG 03-118m

Sample 03-118m is a quartzo-feldspathic host gneiss from southeastern Goodenough Island (Figure 1). At outcrop scale, this gneiss encapsulates mafic eclogite that occurs as a meter-scale lenticular boudin. The eclogite preserves the peak metamorphic assemblage garnet + omphacite + phengite + rutile whereas gneiss sample 03-118m contains an assemblage of quartz + plagioclase + muscovite + biotite + K-feldspar. Zircon crystals from one of these mafic eclogite boudins (sample 03118b in *Monteleone et al.* [2007]), occur as inclusions in garnet and coexist with omphacite in the rock matrix. These zircons yielded a SIMS concordia intercept $^{206}Pb/^{238}U$ age of 2.09 ± 0.49 Ma (through regression of common-Pb uncorrected data with unpinned upper intercept; mean square of weighted deviates [MSWD] = 3.3) [*Monteleone et al.*, 2007]. Trace element data and the coexistence of the dated zircons with omphacite as inclusions in garnet, was used to interpret this U-Pb age as the time of eclogite facies metamorphism, with the authors noting that zircon growth under amphibolite facies conditions cannot be ruled out. Zirconium-in-rutile thermometry for this mafic eclogite gave temperatures ranging from 677 to 817°C, and jadeite barometry gave minimum pressures of 14 kbar [*Monteleone et al.*, 2007]. Zircons extracted from the host gneiss examined in this study (PNG 03-118m) range in length from 100 to 200 μm, are prismatic to acicular, and exhibit oscillatory zoned metamict cores mantled by dark CL rims of variable thickness and up to 5 μm in wide (e.g., Figure 2).

2.2.2. Host Gneiss From the Coesite Eclogite Locality: PNG 08-10g

Sample 08-10g is a quartzo-feldspathic gneiss containing quartz + plagioclase + muscovite + biotite from the coesite eclogite locality (Figure 1) [*Baldwin et al.*, 2008]. The coesite eclogite preserves the peak (U)HP mineral assemblage (clinopyroxene+ garnet+ phengite+ coesite + quartz- + hornblende + zoisite + apatite + rutile + zircon; sample 89321 in *Monteleone et al.* [2007], *Baldwin et al.* [2008], and *Zirakparvar et al.* [2011]). A $^{206}Pb/^{238}U$ age of 7.9 ± 1.9 Ma (regression with unpinned upper intercept) based on in situ SIMS U-Pb analysis of zircon in garnet [*Monteleone et al.*, 2007], and a Lu-Hf garnet age of 7.1 ± 0.7 Ma [*Zirakparvar et al.*, 2011] have both been interpreted to record crystallization of this coesite eclogite at (U)HP conditions. The amphibolite rind of the coesite-bearing eclogite yielded an older $^{40}Ar/^{39}Ar$

amphibole inverse isochron age of 9.83 Ma (sample 89321 in *Baldwin et al.* [1993]). The presence of phengite and amphibole, as well as a muscovite $^{40}Ar/^{39}Ar$ age of 3.52 ± 0.10 Ma, from the same locality (sample 89320 in *Baldwin et al.* [1993]), indicates that hydrous phases were present throughout the evolution of this (U)HP terrane.

Mafic eclogite (sample PNG 08-10f in *Brownlee et al.* [2011] and *Gordon et al.* [2012]), occurs as a boudin within host gneiss sample PNG 08-10g. Although coesite has yet to be documented within this mafic eclogite sample, recent work by *Gordon et al.* [2012] reports a range of in situ laser ablation-inductively coupled plasma-mass spectrometry (LA-ICP-MS) $^{206}Pb/^{238}U$ zircon ages of 9.1 ± 0.6 to 3.8 ± 1.0 Ma in the retrogressed part of this eclogite and 7.4 ± 1.1 to 4.1 ± 1.3 Ma in the "fresh" part of the eclogite, with no inheritance reported. *Gordon et al.* [2012] also report chemical abrasion-thermal ionization mass spectrometry (CA-TIMS) $^{206}Pb/^{238}U$ ages between 5.82 ± 0.2 and 4.78 ± 0.17 Ma for zircons separated from the mafic eclogite. This data suggests that zircon crystallization in mafic eclogite at the coesite locality occurred over a range of P-T conditions from 9.1 to 3.8 Ma. However, the depths corresponding to zircon crystallization during exhumation are not well known.

Zircons in felsic host gneiss PNG 08-10g are prismatic and acicular, up to ~400 μm in length and ~170 μm in width. All of the zircons in this sample exhibit complex internal zoning (Figure 2). Some of the grains have convoluted metamict cores surrounded by concentrically zoned regions, and others exhibit a completely chaotic internal morphology lacking any discernable patterning. The zircons from this sample lack the conspicuous dark CL overgrowths observed in PNG 03-118 m.

2.2.3. Gneiss in Dome Bounding Shear Zone: PNG 06-21a
Sample PNG 06-21a is from an outcrop of layered quartzo-feldspathic gneiss in the Wakonai shear zone (Figure 1), northern Goodenough Island [e.g., *Baldwin et al.*, 1993; *Hill*, 1994; *Little et al.*, 2011]. Sample PNG 06-21a contains quartz + plagioclase + muscovite + zircon + garnet + chlorite. Integrated $^{40}Ar/^{39}Ar$ ages for a sample in close proximity to 06021a are ~1.5 Ma for white mica, ~1.4 Ma for biotite, and ~1.4 Ma for K-feldspar [*Baldwin et al.*, 1993]. Apatite fission-track dating for rocks in the Wakonai shear zone yielded ages of ~0.8 Ma [*Baldwin et al.*, 1993]. These young $^{40}Ar/^{39}Ar$ and apatite fission track ages indicate that this extensional shear zone has been active throughout the last few Myr and is intrinsically related to the exhumation of (U)HP metamorphic rocks in the western Woodlark Basin.

Sample PNG 06-21a contains both prismatic zircons with lengths of ~60 to ~200 μm and subrounded zircons with diameters of ~30 to ~100 μm. Most of the grains exhibit simple to complex oscillatory magmatic zoning. A thin (e.g., <2 μm) light gray CL overgrowth occurs on some grains from this sample (Figure 2).

3. Secondary Ionization Mass Spectrometry (SIMS) Analytical Methods

Ion microprobe measurements were conducted at the UCLA SIMS lab using the CAMECA ims 1270 high-resolution, high-sensitivity ion microprobe. Resolution of mass interferences within the mass range analyzed was possible due to the instrument's high mass resolution (~4500 m/Δm). The data reported in this paper was collected during three sessions (August 2008, July 2010, and May 2011). The first session consisted of analyses of polished zircon cross sections performed in spot mode (Figure 3a). The second analytical session targeted unpolished zircon grain surfaces (Figure 3b). For the third analytical session, analyses also started at the exterior surface of unpolished zircon grains, but profiles had a longer duration and penetrated up to ~15 μm into the crystal (Figure 3c). Only U-Pb analysis was performed during sessions one and two, whereas Ti, Hf, and Y concentrations were measured in conjunction with U-Pb isotopic data during the third session.

Following extraction from ~2 of host rock using standard protocols, including methylene iodide gravimetric separation, zircons were prepared for SIMS analyses in two ways. For analysis of the polished cross sections, grains were mounted in epoxy along with the zircon standard AS3 [*Paces and Miller*, 1993]. These mounts were polished, exposing the internal surfaces of the grains, prior to the application of a thin coating of carbon for scanning electron microscope (SEM) CL imaging. Prior to SIMS analysis the carbon coating was removed through light polishing, the mount was cleaned with dilute HCl, and then coated with an ~30 nm Au film. For analyses on unpolished grain surfaces zircons were pressed into indium metal along with AS3 zircon standard (1099.1 Ma) [*Paces and Miller*, 1993]. Mounts were cleaned with dilute HCl and also coated

with an $\sim$30 nm Au film. ^{57}Fe and ^{197}Au were analyzed during both types of SIMS analysis to monitor beam overlap onto Fe-rich and Ti-rich inclusions in zircon, and surface-derived contaminants, respectively. The analytical parameters for two types of SIMS analyses and data processing are described below.

3.1. Spot Mode (Sectioned Crystals and Unpolished Rims)

A 12.5 kV primary ^{16}O$^-$ beam with a $\sim$20 nA current and $\sim$25 μm beam diameter was used for zircon excavation. Intensities of monatomic U$^+$, Th$^+$, and Pb$^+$ ions and ^{94}Zr$_2$O$^+$ and UO$^+$ molecular ions were measured with a discrete dynode electron multiplier in peak jumping mode. Individual analyses consisted of 15 cycles. O$_2$ flooding at pressures of 3×10^{-5} Torr was applied to the sample surface to enhance Pb yield. In-house software (ZIPS v. 3.0.4; developed by Chris Coath), was used to correct intensity ratios for drift and relative sensitivity variations using a linear fit in UO$^+$/U$^+$ versus Pb$^+$/U$^+$.

3.2. Depth Profiling

Primary ion beam conditions for long depth profiles (session three) were similar to those described in section 3.1, but depth resolution was enhanced by narrowing the field aperture in the secondary ion path to block ions from the periphery of the analysis crater. In addition to the ion species used in spot mode, the petrogenetically relevant trace elements Ti$^+$, Y$^+$, and HfO$^+$ were added to the analysis mass table. Ti and Hf abundances in zircon reflect crystallization temperature (Hf indirectly because of its enrichment during zircon fractionation which is largely controlled by temperature), whereas Y has similar properties as heavy rare earth element (HREE; albeit being present at higher abundances), and thus potentially can indicate garnet presence [e.g., *Monteleone et al.*, 2007]. Each depth profile consisted of 100 cycles with 15 s count times. Following analysis, pit depths from the depth profiles were determined to be $\sim$15 μm using a KLA-Tencor MicroXAM® optical interferometer at UCLA.

3.3. Data Processing

The significantly longer duration for the depth profile (100 cycles) as compared to the spot-mode analysis (15 cycles) necessitates a different approach to correcting raw data for mass fractionation. Our approach for the depth profiles was to generate four separate depth-dependent mass fractionation factors (i.e., separate mass fractionation corrections for cycles 1–25, 26–50, 51–75, and 75–100). This is in contrast to the single mass fractionation correction applied to all 15 cycles making up the spot-mode analysis. For final calculation of isotopic ratios from the long depth profiles, individual cycles in each of the 25 cycle mass fractionation groups were then subdivided into blocks consisting of five cycles each. The result is that data from the depth profiles is reported as a series of 20 blocks each consisting of five cycles, whereas the data from the spot mode simply consists of all 15 cycles from that analysis. All of the U-Pb relative sensitivity corrections are derived relative to zircon standard AS3.

In order to calculate trace element concentrations (Ti, Hf, and Y) for the depth profile analyses, individual cycles from each depth profile were grouped into blocks of five cycles, creating 20 blocks for each depth profile. This is to facilitate direct comparison between the trace element and U-Pb isotopic data for each depth profile. Because zircon standard AS3 is inhomogeneous with regard to trace element abundances, zircon standard 91,500 [*Liu et al.*, 2010] was used to determine trace element relative sensitivity factors (RSF) relative to ^{94}Zr$_2$O$^+$ assuming stoichiometric Zr abundances in standards and unknown. Data from a depth profile conducted on the 91,500 standard was broken down into 20 blocks, each consisting of five cycles. For each of these five cycle blocks the RSF factors for each element were determined by dividing the measured intensities from the standard by the known concentration of the element in the standard (Ti = 4.5 ± 0.4 ppm; Hf = 6250.0 ± 27.2 ppm; Y = 136 ± 2 ppm) [*Liu et al.*, 2010]. These calculations generated 20 RSF factors (one for each five cycle block) as a function of depth that were then used to calculate concentration values for each of the corresponding five cycle blocks from the unknowns. The depth variation of the RSF factors was <4% for Ti, Hf, Th, and U, and $\sim$8% for AS3 zircons analyzed under the same conditions as the unknowns and yielded the following average (n = 4) concentrations: Ti = 27.4 ± 4.5 ppm, HfO$_2$ = 1.37 ± 0.21 wt %, Y = 2300 ± 600 ppm, and U = 900 ± 600 ppm (Th/U = 0.85 ± 0.4; uncertainties are 1 standard deviation). Positive correlation exists between incompatible trace elements Hf-Y, Hf-U, Y-U, whereas Hf-Ti are negatively correlated. Although AS3 trace element abundances are heterogeneous, our values compare reasonably with previously reported trace element concentrations for AS3 zircons (Ti = 21.6 ppm, HfO$_2$ = 1.20 wt %, U = 360 ppm, Th/U = 0.64) [*Aikman*, 2007; *Black et al.*, 2004].

Table 2. Summary of Ages Determined Using Several Approaches (Models) for the Young Zircon Overgrowths in Samples PNG 03-118m and PNG 06-21a, and All Zircons in PNG 08-10g[a]

	Tera-Wasserburg Regressions		Weighted Means of Individual Ages	
	Model 1: Upper Intercept Fixed at C.L.	Model 2: No Fixed Upper Intercept	Model 3: $^{206}Pb/^{238}U$ Ages	Model 4: T.W. Lower Intercept Ages
PNG 03-118m				
Young blocks of depth profiles (n = 38)	***2.89 ± 0.29 Ma***	No regression possible	3.09 ± 1.27 Ma	1.07 ± 1.85 Ma
	MSWD = 2.2		MSWD = 0.93	MSWD = 3.0
Spot-mode analyses < 5 Ma (n = 19)	2.03 ± 0.34 Ma	1.56 ± 0.37 Ma	2.46 ± 2.39 Ma	1.87 ± 1.51 Ma
	MSWD = 6.5	MSWD = 6.6	MSWD = 3.6	MSWD = 1.7
PNG 08-10g				
All blocks of depth profile 1 and 2 (n = 40)	***3.66 ± 0.13 Ma***	No regression possible	3.60 ± 0.78 Ma	3.53 ± 0.80 Ma
	MSWD = 1.6		MSWD = 0.34	MSWD = 0.38
All spot-mode analyses (n = 32)	4.20 ± 0.17 Ma	4.02 ± 0.22 Ma	4.59 ± 3.05 Ma	4.03 ± 0.94Ma
	MSWD = 3.4	MSWD = 3.5	MSWD = 8.0	MSWD = 0.6
PNG 06-21a				
Young blocks of depth profiles (n = 4)	***2.77 ± 0.99 Ma***	No regression possible	2.66 ± 1.52 Ma	2.54 ± 3.00 Ma
	MSWD = 4.6		MSWD = 1.1	MSWD = 4.6
Spot-mode analyses < 5 Ma (n = 7)	4.8 ± 0.61 Ma	No regression possible	4.44 ± 3.50 Ma	4.29 ± 2.25 Ma
	MSWD = 9.1		MSWD = 9	MSWD = 2.9

[a]Column 1: model 1 ages, which are the concordia intercept ages obtained when the analytical data are regressed together on a Tera-Wasserburg Concordia with an upper intercept value fixed at a common $^{207}Pb/^{206}Pb$ value (C.L.) of 0.8283 ± 0.05 [*Sanudo-Wilhemy and Flegal*, 1994]; Column 2: model 2 ages, which are the concordia intercept ages where there is no fixed upper intercept. Column 3: model 3 ages, which are the weighted mean of individual $^{206}Pb/^{238}U$ ages from each sample; Column 4: model 4 ages, which are the weighted mean of individual lower intercept ages. These model 4 lower intercept ages are determined by regressing the ^{207}Pb corrected $^{238}U/^{206}Pb$ and $^{207}Pb/^{206}Pb$ isotopic ratios of the individual unknowns on a Tera-Wasserburg diagram with a *y* axis intercept value that is fixed at the aforementioned common $^{207}Pb/^{206}Pb$ value. The concordia intercept of the regression line between the fixed $^{207}Pb/^{206}Pb$ value and the $^{238}U/^{206}Pb$ and $^{207}Pb/^{206}Pb$ ratios of the unknowns yields a model $^{206}Pb/^{238}U$ age, which are then used in the calculation of the weighted mean model 4 age. The uncertainty on the model 3 and 4 ages is determined by addition of the weighted average uncertainty with the square root of the MSWD value for the weighted average. This is done to account for excess scatter. Note that the significance of these different ages varies from sample to sample, and that the selection of the model age best approximating zircon crystallization (indicated by bold-italic font in the table) is specific to considerations for each sample.

4. Results

The U-Pb isotopic ratios of young zircons are very sensitive to common lead corrections and applying a conventional ^{204}Pb-based common lead correction to the $^{238}U/^{206}Pb$ isotopic ratios of the youngest (e.g., <5 Ma) zircons analyzed in this study introduces unacceptably large uncertainties. For this reason, all of the $^{238}U/^{206}Pb$ isotopic ratios of the zircons were only corrected for common lead using ^{207}Pb, rationalizing that concordance can reasonably be presumed because of the young age and comparatively low U in the zircons [e.g., *Baldwin and Ireland*, 1995; *Schmitt et al.*, 2003]. U-Pb data and ages are reported in a variety of ways. Table 2 summarizes Pliocene U-Pb ages determined in spot and depth-profiling modes when various zircon populations from each sample are grouped together (see below for explanation of selection criteria and age determinations). Table 3 reports U-Pb results for the spot-mode analyses, including zircons that yielded inherited ages not used in the age calculations reported in Table 1. Table 4 reports analytical results from the depth profiles including U-Pb isotopic data and Ti, Hf, and Y concentrations. For the depth profile analyses, Ti concentrations are used to calculate model zircon crystallization temperatures based on the calibration (at 1 GPa): $T(°C) = (-1/((Log (Ti_{conc}) - 5.711)/4800)) - 273.15$ [*Ferry and Watson*, 2007]. The U-Pb data is also used in the construction of Figure 4, comparing the $^{206}Pb/^{238}U$ ages from the spot mode (shown here as probability density curves) with the depth profile analyses (shown here as age versus depth), and Figure 5, containing Tera-Wasserburg concordia diagrams for the young zircon populations determined in both analytical modes.

Model 1 ages reported in Table 2 are the concordia intercept ages obtained when the analytical data from the specified population are regressed together on a Tera-Wasserburg plot with a *y* axis intercept fixed at a common $^{207}Pb/^{206}Pb$ composition of 0.8283 ± 0.05 [*Sanudo-Wilhemy and Flegal*, 1994]. Model 2 ages are the concordia intercept ages where there is no fixed *y* axis intercept. Model 3 ages in Table 2 are the weighted mean of individual $^{206}Pb/^{238}U$ ages for the specified population from each sample, whereas model 4 ages are the weighted mean of individual concordia intercept ages for the same population. Model 4 ages are determined by regressing the ^{207}Pb corrected $^{238}U/^{206}Pb$ and $^{207}Pb/^{206}Pb$ isotopic ratios of the individual unknowns on a Tera-Wasserburg diagram with a *y* axis intercept value that is fixed at the aforementioned common $^{207}Pb/^{206}Pb$ value. The concordia intercept of the regression line between the fixed $^{207}Pb/^{206}Pb$ value and the

Table 3. Summary of U-Pb Isotopic Data and Ages for the Spot-Mode Analyses Conducted During This Study[a]

		$^{207}Pb*/^{206}Pb*$	+/-	$^{207}Pb*/^{235}U$	+/-	$^{206}Pb*/^{238}U$	+/-	$^{206}Pb/^{238}U$ Age (Ma)	+/-
PNG 03-118m in spot mode:			1 s.e.		1 s.e.		1 s.e.		1 s.e.
03118_z1@1	P	0.063	0.003	0.111	0.006	0.0127	0.0007	81.4	4.2
03118m_mounted_1	UP	0.22	0.05	0.011	0.002	0.00038	0.00002	2.4	0.1
03118_z2@1	P	0.056	0.002	0.109	0.006	0.0141	0.0007	90.0	4.5
03118_z2@2	P	0.053	0.002	0.100	0.005	0.0136	0.0007	87.0	4.4
03118_z2@3	P	0.051	0.001	0.106	0.004	0.0153	0.0005	97.6	3.5
03118m_mounted_2	UP	0.24	0.05	0.008	0.002	0.00023	0.00001	1.5	0.1
03118_z1@2	P	0.14	0.01	0.15	0.01	0.0078	0.0005	49.9	3.5
03118_z3@1	P	0.054	0.001	0.106	0.006	0.0142	0.0006	90.8	4.0
03118_z3@2	P	0.064	0.004	0.079	0.005	0.0090	0.0004	57.5	2.5
03118m_mounted_3	UP	0.053	0.003	0.109	0.007	0.0149	0.0011	95.2	7.3
03118_z4@1	P	0.063	0.003	0.129	0.007	0.0149	0.0007	95.3	4.6
03118_z5@1	P	0.10	0.01	0.15	0.01	0.0112	0.0007	71.7	4.4
03118m_mounted_5	UP	0.25	0.04	0.017	0.002	0.00051	0.00003	3.3	0.2
03118_z6@1	P	0.049	0.001	0.117	0.007	0.0173	0.0008	110	5
03118_z6@2	P	0.049	0.001	0.103	0.005	0.0153	0.0007	97.7	4.7
03118_z6@3	P	0.56	0.04	0.36	0.03	0.0046	0.0005	29.9	3.1
03118_z7@1	P	0.053	0.001	0.079	0.004	0.0108	0.0004	69.2	2.9
03118m_mounted_7	UP	0.57	0.07	0.08	0.01	0.0011	0.0001	6.8	0.5
03118z9@1	P	0.062	0.004	0.102	0.009	0.0120	0.0005	76.6	3.2
03118z10@1	P	0.052	0.002	0.099	0.006	0.0139	0.0006	89.2	3.7
03118m_separate_1	UP	0.59	0.06	0.087	0.008	0.0011	0.0001	6.8	0.4
03118m_separate_2	UP	0.49	0.08	0.055	0.006	0.0008	0.0001	5.3	0.5
03118m_separate_3	UP	0.25	0.05	0.011	0.002	0.00032	0.00002	2.0	0.1
03118m_separate_4	UP	0.79	0.03	0.41	0.04	0.0037	0.0003	24.1	2.1
03118m_separate_5	UP	0.46	0.04	0.08	0.01	0.0013	0.0001	8.2	0.7
03118m_separate_6	UP	0.26	0.05	0.017	0.003	0.00048	0.00003	3.1	0.2
03118m_separate_7	UP	0.09	0.01	0.15	0.02	0.0119	0.0005	76.5	3.3
03118m_separate_9	UP	0.62	0.05	0.16	0.03	0.0019	0.0002	12.0	1.3
03118m_separate_10	UP	0.69	0.09	0.21	0.03	0.0022	0.0002	14.4	1.4
03118m_separate_11	UP	0.6	0.1	0.051	0.008	0.0006	0.0001	3.8	0.4
03118m_separate_12	UP	0.62	0.09	0.127	0.016	0.0015	0.0001	9.7	0.7
03118m_separate_13	UP	0.59	0.08	0.10	0.01	0.0012	0.0001	7.7	0.7
03118m_separate_14	UP	0.08	0.01	0.146	0.009	0.0125	0.0008	80.0	5.1
03118m_separate_15	UP	0.37	0.06	0.030	0.004	0.00060	0.00004	3.9	0.3
03118m_separate_17	UP	0.07	0.02	0.21	0.13	0.0205	0.0085	131	54
03118m_separate_18	UP	0.49	0.09	0.031	0.006	0.00046	0.00004	3.0	0.2
03118m_separate_19	UP	0.10	0.01	0.005	0.001	0.00041	0.00001	2.6	0.1
03118m_separate_21	UP	0.38	0.06	0.018	0.003	0.00035	0.00002	2.2	0.2
03118m_separate_22	UP	0.51	0.09	0.036	0.006	0.00052	0.00004	3.4	0.2
03118m_separate_24	UP	0.26	0.04	0.019	0.004	0.00054	0.00004	3.5	0.3
03118m_separate_25	UP	0.31	0.07	0.020	0.004	0.00045	0.00002	2.9	0.2
PNG 08-10g in spot mode:			1 s.e.		1 s.e.		1 s.e.		1 s.e.
08010z1@1	P	0.13	0.02	0.012	0.002	0.00068	0.00004	4.4	0.2
08010g_mounted_1	UP	0.13	0.02	0.012	0.002	0.00067	0.00003	4.3	0.2
08010g_mounted_1b	UP	0.08	0.01	0.010	0.002	0.0008	0.0001	5.5	0.8
08010z2@1	P	0.09	0.02	0.009	0.002	0.00069	0.00003	4.4	0.2
08010z2@2	P	0.06	0.00	0.0058	0.0003	0.00076	0.00002	4.9	0.2
08010g_mounted_2	UP	0.09	0.01	0.010	0.001	0.00078	0.00004	5.0	0.3
08010z3@1	P	0.31	0.04	0.049	0.008	0.00117	0.00009	7.5	0.6
08010z4@1	P	0.059	0.003	0.0056	0.0004	0.00069	0.00002	4.4	0.2
08010_z5@1	P	0.12	0.01	0.012	0.001	0.00072	0.00003	4.6	0.2
08010_z5@2	P	0.18	0.02	0.019	0.003	0.00077	0.00004	5.0	0.3
08010_z6@1	P	0.12	0.01	0.011	0.001	0.00070	0.00004	4.5	0.2
08010_z6@2	P	0.15	0.01	0.013	0.002	0.00067	0.00002	4.3	0.1
08010g_mounted_6	UP	0.060	0.005	0.004	0.001	0.00052	0.00003	3.3	0.2
08010_z8@1	P	0.32	0.05	0.033	0.006	0.00074	0.00005	4.8	0.3
08010_z9@1	P	0.30	0.03	0.038	0.005	0.00090	0.00006	5.8	0.4
08010_z9@2	P	0.26	0.03	0.032	0.005	0.00089	0.00007	5.7	0.4
08010g_separate_3	UP	0.07	0.01	0.007	0.001	0.00069	0.00003	4.5	0.2
08010g_separate_5	UP	0.34	0.02	0.050	0.006	0.00105	0.00007	6.8	0.4
08010g_separate_6	UP	0.07	0.01	0.006	0.001	0.00061	0.00002	3.9	0.2

Table 3. (continued)

		$^{207}Pb*/^{206}Pb*$	+/-	$^{207}Pb*/^{235}U$	+/-	$^{206}Pb*/^{238}U$	+/-	$^{206}Pb/^{238}U$ Age (Ma)	+/-
08010g_separate_8	UP	0.25	0.03	0.032	0.005	0.00091	0.00006	5.9	0.4
08010g_separate_9	UP	0.14	0.03	0.019	0.003	0.0010	0.0001	6.2	0.9
08010g_separate_10	UP	0.20	0.02	0.023	0.003	0.00081	0.00004	5.2	0.3
08010g_separate_11	UP	0.23	0.03	0.025	0.003	0.00080	0.00004	5.2	0.3
08010g_separate_12	UP	0.09	0.01	0.009	0.001	0.00076	0.00003	4.9	0.2
08010g_separate_13b	UP	0.22	0.03	0.025	0.003	0.00082	0.00004	5.3	0.3
08010g_separate_14	UP	0.10	0.01	0.011	0.001	0.00083	0.00005	5.3	0.3
08010g_separate_15	UP	0.14	0.02	0.013	0.002	0.00068	0.00003	4.4	0.2
08010g_separate_17	UP	0.10	0.01	0.009	0.001	0.00068	0.00003	4.4	0.2
08010g_separate_18	UP	0.17	0.02	0.016	0.002	0.00070	0.00004	4.5	0.2
08010g_separate_19	UP	0.20	0.05	0.023	0.006	0.00082	0.00006	5.3	0.4
08010g_separate_20	UP	0.10	0.01	0.010	0.001	0.00067	0.00003	4.3	0.2
08010g_separate_22	UP	0.12	0.02	0.010	0.001	0.00060	0.00003	3.9	0.2
PNG 06-21a in spot mode:			1 s.e.		1 s.e.		1 s.e.		1 s.e.
06021_z1@1	P	0.051	0.001	0.072	0.004	0.0103	0.0004	65.9	2.6
06021_z1@2	P	0.20	0.02	0.017	0.002	0.00062	0.00004	4.0	0.2
06021_z3@3	P	0.051	0.001	0.094	0.004	0.0134	0.0005	86.0	3.5
06021_z4@1	P	0.065	0.005	0.007	0.001	0.00077	0.00003	4.9	0.2
06021_z5@1	P	0.051	0.001	0.041	0.002	0.0059	0.0002	38.0	1.3
06021_z5@2	P	0.065	0.004	0.0064	0.0005	0.00071	0.00003	4.6	0.2
06021_z6@1	P	0.058	0.003	0.098	0.006	0.0122	0.0005	78.4	3.3
06021_z6@2	P	0.056	0.002	0.087	0.004	0.0112	0.0004	71.9	2.3
06021_z6@3	P	0.054	0.002	0.082	0.006	0.0110	0.0005	70.2	3.3
06021_z7@1	P	0.076	0.004	0.18	0.01	0.017	0.001	109	6
06021_z7@2	P	0.059	0.003	0.15	0.01	0.019	0.001	119	8
06021_z7@3	P	0.060	0.004	0.073	0.008	0.0089	0.0004	56.9	2.6
06021_z7@4	P	0.085	0.007	0.010	0.001	0.0008	0.0001	5.3	0.3
06021_z7@5	P	0.049	0.001	0.059	0.003	0.0087	0.0003	55.6	1.9
06021_z8@1	P	0.083	0.001	1.52	0.05	0.133	0.005	803	27
06021_z8@2	P	0.084	0.001	2.1	0.1	0.184	0.008	1090	50
06021_z8@3	P	0.084	0.001	2.14	0.10	0.185	0.009	1090	52
06021_z8@4	P	0.049	0.001	0.084	0.006	0.0123	0.0007	79.0	4.6
06021_z8@5	P	0.051	0.002	0.091	0.005	0.0128	0.0005	81.8	3.1
06021_z9@1	P	0.070	0.001	0.34	0.01	0.035	0.001	224	7
06021_z11@1	P	0.054	0.001	0.115	0.005	0.0156	0.0006	99.6	3.7
06021_z11@2	P	0.054	0.001	0.186	0.009	0.023	0.001	159	7
06021_z12@1	P	0.093	0.001	1.05	0.04	0.082	0.003	507	21
06021_z12@2	P	0.050	0.002	0.115	0.009	0.0168	0.0009	107	6
06021_z13@1	P	0.053	0.002	0.096	0.004	0.0130	0.0006	83.1	3.6
06021_z14@1	P	0.052	0.002	0.097	0.005	0.0134	0.0006	85.6	3.7
06021_z11@3	P	0.067	0.005	0.0064	0.0005	0.00069	0.00003	4.5	0.2
06021_z13@2	P	0.058	0.003	0.0047	0.0003	0.00059	0.00002	3.8	0.1
06021_z15@1	P	0.065	0.004	0.17	0.01	0.019	0.001	119	5
06021_z16@1	P	0.058	0.002	0.0062	0.0003	0.00078	0.00003	5.0	0.2

[a]"P" and "UP" following the analysis name denote spot-mode analyses on polished and unpolished surfaces, respectively. Refer to section 4 for explanation of common lead correction.

$^{238}U/^{206}Pb$ and $^{207}Pb/^{206}Pb$ ratios of the unknowns yields a model $^{206}Pb/^{238}U$ age, which are then used in the calculation of the weighted mean age (i.e., model 4 age). The uncertainties for the model 3 and 4 ages have been scaled by the square root of the MSWD to account for excess scatter, whereas uncertainty in the model 1 and 2 ages are simply quoted at the 95% confidence interval. Whereas these different common-Pb correction schemes are expected to converge to the same calculated age, the individual model assumptions (in particular the relaxation of any constraints on common Pb) can introduce significant differences in the apparent ages. We deem it prudent to present the full range of model ages (Table 2) for each sample, but emphasize that occasional model age divergence does not impact any of our conclusions.

For the depth profiles, depth is obtained by dividing the 20 blocks in each depth profile analysis by the ∼15 μm depth of the analysis crater; each analytical block corresponds to approximately 0.75 μm depth. The error bars for each ∼0.75 μm thick analytical block for the U-Pb ages from the depth profiles in Figure 4 are the within-run ± 1σ standard error of the mean. The error bars for each ∼0.75 μm thick analytical block for the

Table 4. Summary of U-Pb Ages and Trace Element Concentrations for the SIMS Depth Profiles Conducted in This Study[a]

Depth Interval	blk	$^{207}Pb*/^{206}Pb*$	+/-	$^{207}Pb*/^{235}U$	+/-	$^{206}Pb*/^{238}U$	+/-	$^{206}Pb/^{238}U$ Age (Ma)	+/-	Ti ppm	Ti °C	Hf ppm	Y ppm
Sample 03118m Depth profile 1			1 s.e.		1 s.e.		1 s.e.		1 s.e.				
0.0 to 0.75 μm	1	0.2	0.1	0.01	0.01	0.0005	0.0001	3.1	0.9	3.8	663	16400	154
0.75 to 1.5 μm	2	0.3	0.1	0.018	0.009	0.0004	0.0001	2.7	0.9	3.9	664	16000	110
1.5 to 2.25 μm	3	0.3	0.2	0.01	0.01	0.0003	0.0001	2.1	0.9	3.4	654	15600	86
2.25 to 3.0 μm	4	0.3	0.2	0.02	0.01	0.0005	0.0002	3.5	1.4	3.1	649	15500	73
3.0 to 3.75 μm	5	0.2	0.1	0.02	0.01	0.0006	0.0002	3.8	1.4	3.0	645	15600	63
3.75 to 4.5 μm	6	0.7	0.4	0.025	0.009	0.0003	0.0001	1.6	0.6	2.6	635	15700	57
4.5 to 5.25 μm	7	0.1	0.1	0.007	0.005	0.0007	0.0002	4.5	1.3	2.4	627	15600	52
5.25 to 6.0 μm	8	0.5	0.4	0.03	0.02	0.0004	0.0001	2.6	1.0	2.2	622	16200	49
6.0 to 6.75 μm	9	0.1	0.1	0.012	0.009	0.0006	0.0001	3.9	0.8	1.8	609	15700	43
6.75 to 7.5 μm	10	0.2	0.3	0.01	0.02	0.0005	0.0002	3.1	1.4	1.8	608	16600	46
7.5 to 8.25 μm	11	0.2	0.2	0.01	0.01	0.0004	0.0002	2.6	1.0	1.7	603	16300	40
8.25 to 9.0 μm	12	0.2	0.1	0.015	0.009	0.0006	0.0002	4.1	1.3	1.5	596	16200	39
9.0 to 9.75 μm	13	0.2	0.2	0.013	0.009	0.0005	0.0002	3.2	1.4	1.6	598	16100	37
9.75 to 10.50 μm	14	0.2	0.1	0.02	0.02	0.0008	0.0003	5.5	1.9	1.6	600	16400	36
10.5 to 11.25 μm	15	0.1	0.1	0.007	0.007	0.0006	0.0004	3.8	2.3	1.6	598	16100	33
11.25 to 12.0 μm	16	0.2	0.1	0.05	0.02	0.0019	0.0009	12.4	5.9	1.5	593	16000	39
12.0 to 12.75 μm	17	0.06	0.02	0.04	0.01	0.0042	0.0008	27.0	4.9	1.5	597	16400	108
12.75 to 13.5 μm	18	0.05	0.01	0.05	0.01	0.007	0.001	43.3	7.9	1.5	595	15900	183
13.5 to 14.25 μm	19	0.04	0.01	0.03	0.01	0.007	0.001	45.2	8.0	1.6	598	16300	275
14.25 to 15.0 μm	20	0.05	0.01	0.06	0.01	0.008	0.001	54.5	9.0	1.7	605	16100	350
Sample 03118m Depth profile 2			1 s.e.		1 s.e.		1 s.e.		1 s.e.				
0.0 to 0.75 μm	1	0.10	0.02	0.006	0.001	0.0004	0.0001	2.7	0.6	1.8	609	17100	1540
0.75 to 1.5 μm	2	0.05	0.02	0.003	0.001	0.0004	0.0001	2.3	0.6	2.0	616	17900	1520
1.5 to 2.25 μm	3	0.06	0.02	0.004	0.001	0.0004	0.0001	2.7	0.6	1.9	611	17400	1440
2.25 to 3.0 μm	4	0.05	0.02	0.003	0.001	0.0005	0.0001	3.1	0.8	1.9	613	16800	1350
3.0 to 3.75 μm	5	0.06	0.02	0.003	0.002	0.0004	0.0001	2.7	0.7	2.0	614	17100	1330
3.75 to 4.5 μm	6	0.08	0.02	0.004	0.002	0.0004	0.0002	2.7	1.0	2.0	617	17200	1040
4.5 to 5.25 μm	7	0.07	0.03	0.004	0.002	0.0005	0.0002	3.1	1.2	2.1	618	17200	909
5.25 to 6.0 μm	8	0.09	0.04	0.005	0.003	0.0004	0.0002	2.8	1.0	2.2	621	17800	816
6.0 to 6.75 μm	9	0.03	0.03	0.002	0.001	0.0004	0.0001	2.8	1.0	2.1	619	17400	648
6.75 to 7.5 μm	10	0.05	0.03	0.003	0.002	0.0005	0.0001	3.2	0.9	2.0	617	17800	544
7.5 to 8.25 μm	11	0.05	0.02	0.003	0.002	0.0004	0.0001	2.8	0.9	2.1	618	17300	388
8.25 to 9.0 μm	12	0.05	0.01	0.008	0.003	0.0013	0.0004	8.1	2.4	2.4	627	17400	426
9.0 to 9.75 μm	13	0.05	0.01	0.015	0.006	0.0023	0.0006	14.5	3.9	2.7	638	17100	491
9.75 to 10.50 μm	14	0.04	0.01	0.024	0.008	0.004	0.001	27.2	8.1	3.4	654	17200	732
10.5 to 11.25 μm	15	0.06	0.02	0.04	0.01	0.005	0.001	31.9	9.6	3.5	657.	16800	871
11.25 to 12.0 μm	16	0.06	0.01	0.042	0.007	0.0054	0.0008	34.7	5.2	3.6	659	16200	914
12.0 to 12.75 μm	17	0.05	0.01	0.044	0.008	0.0066	0.0009	42.4	6.1	3.5	658	15900	1020
12.75 to 13.5 μm	18	0.05	0.01	0.05	0.01	0.007	0.001	45.9	6.7	3.8	662	15800	1150
13.5 to 14.25 μm	19	0.05	0.01	0.053	0.009	0.008	0.001	51.6	7.7	4.0	667	15400	1320
14.25 to 15.0 μm	20	0.042	0.004	0.046	0.008	0.008	0.001	51.2	7.7	4.1	670	15600	1570
Sample 03118m Depth profile 3	Blk		1 s.e.		1 s.e.		1 s.e.		1 s.e.				
0.0 to 0.75 μm	1	0.4	0.2	0.04	0.02	0.0007	0.0002	4.7	1.2	3.6	659	15100	94
0.75 to 1.5 μm	2	0.1	0.1	0.01	0.01	0.0005	0.0003	3.1	1.7	2.4	628	15000	62
1.5 to 2.25 μm	3	0.6	0.4	0.05	0.02	0.0006	0.0003	3.9	1.7	1.9	612	15100	48
2.25 to 3.0 μm	4	0.7	0.4	0.05	0.03	0.0005	0.0003	3.1	1.9	1.6	599	14700	38
3.0 to 3.75 μm	5	0.2	0.2	0.02	0.02	0.0008	0.0003	5.0	1.8	1.5	594	14900	34
3.75 to 4.5 μm	6	0.3	0.2	0.03	0.02	0.0007	0.0004	4.7	2.5	1.4	590	15300	32
4.5 to 5.25 μm	7	0.02	0.02	0.02	0.02	0.007	0.002	47.3	14.8	1.4	591	14600	87
5.25 to 6.0 μm	8	0.05	0.01	0.10	0.03	0.013	0.003	84.3	19.7	2.2	621	15000	583
6.0 to 6.75 μm	9	0.050	0.004	0.09	0.02	0.013	0.003	83.6	17.0	2.5	631	15100	978
6.75 to 7.5 μm	10	0.04	0.01	0.08	0.02	0.014	0.003	89.6	19.1	2.7	637	15400	1440
7.5 to 8.25 μm	11	0.051	0.004	0.10	0.03	0.014	0.004	92.4	27.0	3.2	649	15300	1570
8.25 to 9.0 μm	12	0.05	0.01	0.11	0.03	0.015	0.004	95.2	28.3	3.1	647	15200	1800
9.0 to 9.75 μm	13	0.050	0.004	0.10	0.03	0.015	0.004	93.8	28.5	3.2	651	15600	1900
9.75 to 10.50 μm	14	0.053	0.003	0.11	0.03	0.015	0.004	94.7	27.8	3.3	652	15600	1900
10.5 to 11.25 μm	15	0.05	0.01	0.10	0.03	0.015	0.004	96.5	27.7	3.1	647	15600	1930
11.25 to 12.0 μm	16	0.047	0.002	0.09	0.01	0.014	0.002	88.6	11.2	3.0	646	15900	1970
12.0 to 12.75 μm	17	0.052	0.003	0.10	0.01	0.014	0.002	86.9	11.5	3.3	651	17500	2360
12.75 to 13.5 μm	18	0.049	0.002	0.09	0.01	0.013	0.002	85.1	11.4	3.2	650	17100	2530
13.5 to 14.25 μm	19	0.050	0.002	0.09	0.01	0.014	0.002	86.8	11.7	3.1	648	17100	2680
14.25 to 15.0 μm	20	0.050	0.004	0.09	0.01	0.013	0.002	84.9	12.1	3.2	650	17900	2910

Table 4. (continued)

Depth Interval	blk	$^{207}Pb*/^{206}Pb*$	+/-	$^{207}Pb*/^{235}U$	+/-	$^{206}Pb*/^{238}U$	+/-	$^{206}Pb/^{238}U$ Age (Ma)	+/-	Ti ppm	Ti °C	Hf ppm	Y ppm
Sample 03118m Depth profile 5													
			1 s.e.		1 s.e.		1 s.e.		1 s.e.				
0.0 to 0.75 μm	1	0.40	0.08	0.05	0.01	0.0008	0.0001	5.4	0.7	3.9	665	14800	88
0.75 to 1.5 μm	2	0.5	0.2	0.04	0.01	0.0007	0.0002	4.3	1.1	4.0	668	14800	67
1.5 to 2.25 μm	3	0.4	0.2	0.04	0.02	0.0007	0.0003	4.4	1.7	3.0	645	14400	63
2.25 to 3.0 μm	4	0.29	0.09	0.04	0.02	0.0010	0.0003	6.3	1.8	2.9	642	15000	62
3.0 to 3.75 μm	5					0.0005	0.0003	3.4	1.7	2.8	639	15200	59
3.75 to 4.5 μm	6	1.2	0.6	0.07	0.04	0.0004	0.0003	2.6	2.2	2.5	631	15200	58
4.5 to 5.25 μm	7	0.4	0.2	0.03	0.02	0.0007	0.0003	4.6	2.1	2.3	624	15100	58
5.25 to 6.0 μm	8	0.08	0.02	0.06	0.02	0.005	0.002	31.6	11.0	2.4	627	16000	104
6.0 to 6.75 μm	9	0.05	0.01	0.07	0.02	0.010	0.002	62.0	13.5	2.4	628	16200	335
6.75 to 7.5 μm	10	0.05	0.01	0.07	0.02	0.010	0.002	66.6	13.1	2.6	635	16500	585
7.5 to 8.25 μm	11	0.05	0.01	0.07	0.02	0.009	0.002	60.8	14.9	2.4	629	17400	659
8.25 to 9.0 μm	12	0.05	0.00	0.07	0.02	0.010	0.003	64.1	16.1	2.6	634	17900	901
9.0 to 9.75 μm	13	0.05	0.01	0.07	0.02	0.010	0.002	62.9	15.9	2.7	636	18000	1090
9.75 to 10.50 μm	14	0.05	0.01	0.08	0.02	0.011	0.003	68.0	19.4	3.5	656	18800	1760
10.5 to 11.25 μm	15	0.06	0.01	0.08	0.03	0.010	0.003	67.1	20.0	4.5	676	19100	3390
11.25 to 12.0 μm	16	0.057	0.005	0.07	0.01	0.009	0.001	57.1	7.9	5.5	694	19000	4340
12.0 to 12.75 μm	17	0.058	0.002	0.07	0.01	0.009	0.001	58.3	7.8	6.2	703	20000	5180
12.75 to 13.5 μm	18	0.055	0.002	0.07	0.01	0.010	0.001	62.8	8.2	5.3	690	19200	4560
13.5 to 14.25 μm	19	0.051	0.004	0.07	0.01	0.010	0.001	66.2	8.4	5.1	687	18800	3970
14.25 to 15.0 μm	20	0.051	0.003	0.07	0.01	0.010	0.001	65.4	9.0	4.8	682	19400	3640
Sample 08010g Depth profile 1													
			1 s.e.		1 s.e.		1 s.e.		1 s.e.				
0.0 to 0.75 μm	1	0.06	0.02	0.007	0.002	0.0008	0.0002	5.0	1.0	1.9	611	14200	355
0.75 to 1.5 μm	2	0.09	0.03	0.008	0.003	0.0007	0.0001	4.3	0.9	1.7	604	15100	303
1.5 to 2.25 μm	3	0.03	0.02	0.003	0.002	0.0007	0.0001	4.7	0.9	1.6	599	15800	266
2.25 to 3.0 μm	4	0.02	0.01	0.002	0.001	0.0007	0.0001	4.5	0.9	1.6	598	16400	249
3.0 to 3.75 μm	5	0.04	0.02	0.004	0.002	0.0008	0.0002	5.0	1.1	1.6	600	18200	270
3.75 to 4.5 μm	6	0.05	0.02	0.006	0.003	0.0008	0.0003	5.4	1.9	1.7	603	20000	241
4.5 to 5.25 μm	7	0.04	0.01	0.004	0.002	0.0008	0.0003	5.1	2.0	1.6	599	20400	222
5.25 to 6.0 μm	8	0.03	0.01	0.003	0.002	0.0009	0.0004	6.0	2.4	1.6	601	21000	210
6.0 to 6.75 μm	9	0.11	0.04	0.013	0.007	0.0008	0.0003	5.4	2.2	1.7	603	21100	197
6.75 to 7.5 μm	10	0.08	0.03	0.010	0.005	0.0009	0.0004	5.9	2.6	1.6	598	20500	186
7.5 to 8.25 μm	11	0.09	0.03	0.011	0.006	0.0009	0.0005	5.5	3.1	1.8	608	19400	161
8.25 to 9.0 μm	12	0.05	0.03	0.007	0.006	0.0010	0.0006	6.5	3.8	15	786	18500	360
9.0 to 9.75 μm	13	0.04	0.02	0.005	0.004	0.0009	0.0004	5.7	2.7	112	1040	18100	1240
9.75 to 10.50 μm	14	0.07	0.02	0.007	0.003	0.0007	0.0003	4.7	2.0	212	1150	17400	2040
10.5 to 11.25 μm	15	0.07	0.02	0.008	0.003	0.0007	0.0003	4.7	1.8	261	1190	16600	2530
11.25 to 12.0 μm	16	0.05	0.02	0.005	0.002	0.0006	0.0001	4.1	0.7	319	1220	15400	3110
12.0 to 12.75 μm	17	0.04	0.02	0.004	0.002	0.0006	0.0001	3.9	0.7	369	1250	15600	3630
12.75 to 13.5 μm	18	0.11	0.05	0.008	0.004	0.0006	0.0001	3.5	0.6	393	1270	14900	3800
13.5 to 14.25 μm	19	0.16	0.05	0.015	0.004	0.0007	0.0001	4.3	0.7	419	1280	15000	4060
14.25 to 15.0 μm	20	0.06	0.02	0.005	0.002	0.0006	0.0001	4.0	0.8	426	1290	14700	4140
Sample 08010g Depth profile 2													
			1 s.e.		1 s.e.		1 s.e.		1 s.e.				
0.0 to 0.75 μm	1	0.2	0.1	0.020	0.009	0.0006	0.0001	3.8	0.8	2.2	623	18100	387
0.75 to 1.5 μm	2	0.11	0.04	0.009	0.004	0.0006	0.0001	3.6	0.7	2.0	615	18300	388
1.5 to 2.25 μm	3	0.06	0.02	0.005	0.003	0.0007	0.0001	4.6	0.9	1.8	607	17900	351
2.25 to 3.0 μm	4	0.08	0.02	0.007	0.002	0.0006	0.0001	4.2	0.7	1.6	599	18500	344
3.0 to 3.75 μm	5	0.05	0.02	0.003	0.001	0.00048	0.00008	3.1	0.5	2.5	631	20700	526
3.75 to 4.5 μm	6	0.05	0.02	0.004	0.001	0.0006	0.0001	3.6	0.7	4.1	669	24300	992
4.5 to 5.25 μm	7	0.06	0.01	0.005	0.001	0.00053	0.00009	3.4	0.6	4.8	682	24800	1190
5.25 to 6.0 μm	8	0.06	0.01	0.005	0.001	0.0006	0.0001	3.8	0.6	5.6	695	24900	1490
6.0 to 6.75 μm	9	0.05	0.01	0.0035	0.0009	0.00051	0.00008	3.3	0.5	6.3	705	24400	1890
6.75 to 7.5 μm	10	0.05	0.01	0.0035	0.0008	0.00049	0.00007	3.2	0.5	7.5	721	23500	2410
7.5 to 8.25 μm	11	0.05	0.01	0.004	0.001	0.0006	0.0001	3.6	0.8	10.2	749	22600	3180
8.25 to 9.0 μm	12	0.04	0.01	0.0029	0.0008	0.0005	0.0001	3.3	0.7	12.3	766	21600	3690
9.0 to 9.75 μm	13	0.05	0.01	0.0036	0.0009	0.0006	0.0001	3.6	0.8	13.4	775	21900	3670
9.75 to 10.50 μm	14	0.07	0.02	0.005	0.002	0.0005	0.0001	3.3	0.7	13.4	775	23400	3430
10.5 to 11.25 μm	15	0.05	0.01	0.0040	0.0009	0.0005	0.0001	3.4	0.7	12.5	768	23500	3130
11.25 to 12.0 μm	16	0.05	0.01	0.0038	0.0006	0.00056	0.00007	3.6	0.4	13.3	774	24800	3090
12.0 to 12.75 μm	17	0.05	0.01	0.0041	0.0006	0.00055	0.00007	3.6	0.4	13.7	777	26400	3150
12.75 to 13.5 μm	18	0.06	0.01	0.0041	0.0006	0.00052	0.00007	3.4	0.4	13.6	777	25300	2950
13.5 to 14.25 μm	19	0.06	0.01	0.0042	0.0006	0.00050	0.00006	3.2	0.4	13.8	778	25500	3060

Table 4. (continued)

Depth Interval	blk	$^{207}Pb*/^{206}Pb*$	+/-	$^{207}Pb*/^{235}U$	+/-	$^{206}Pb*/^{238}U$	+/-	$^{206}Pb/^{238}U$ Age (Ma)	+/-	Ti ppm	Ti °C	Hf ppm	Y ppm
			1 s.e.		1 s.e.		1 s.e.		1 s.e.				
14.25 to 15.0 μm	20	0.05	0.01	0.0037	0.0006	0.00053	0.00007	3.4	0.5	15.0	787	26300	3210
Sample 08010g Depth profile 3													
Depth Interval	blk		1 s.e.		1 s.e.		1 s.e.		1 s.e.				
0.0 to 0.75 μm	1	0.11	0.03	0.009	0.003	0.0006	0.0001	3.9	0.8	3.7	660	17200	645
0.75 to 1.5 μm	2	0.08	0.03	0.005	0.002	0.0005	0.0001	3.3	0.7	4.4	674	18600	799
1.5 to 2.25 μm	3	0.07	0.02	0.005	0.002	0.0005	0.0001	3.4	0.7	4.7	681	19200	900
2.25 to 3.0 μm	4	0.04	0.01	0.003	0.001	0.0006	0.0001	4.1	0.7	4.5	678	19700	887
3.0 to 3.75 μm	5	0.06	0.02	0.005	0.002	0.0007	0.0001	4.2	0.7	4.3	674	20300	868
3.75 to 4.5 μm	6	0.07	0.02	0.005	0.001	0.0006	0.0001	3.7	0.7	3.9	665	20800	851
4.5 to 5.25 μm	7	0.09	0.02	0.007	0.002	0.0006	0.0001	3.6	0.7	3.6	658	20000	793
5.25 to 6.0 μm	8	0.04	0.01	0.003	0.001	0.0006	0.0001	3.8	0.7	3.7	661	20100	778
6.0 to 6.75 μm	9	0.05	0.02	0.004	0.001	0.0006	0.0001	3.6	0.7	3.5	657	20400	828
6.75 to 7.5 μm	10	0.05	0.03	0.004	0.002	0.0006	0.0001	3.7	0.8	3.4	655	20600	820
7.5 to 8.25 μm	11	0.07	0.02	0.005	0.002	0.0006	0.0002	3.7	1.1	3.9	665	19300	691
8.25 to 9.0 μm	12	0.05	0.02	0.004	0.002	0.0006	0.0002	3.7	1.1	4.2	671	19200	632
9.0 to 9.75 μm	13	0.06	0.01	0.005	0.002	0.0006	0.0002	4.2	1.2	4.4	674	19200	576
9.75 to 10.50 μm	14	0.04	0.01	0.004	0.001	0.0006	0.0002	4.0	1.2	4.3	673	18900	510
10.5 to 11.25 μm	15	0.05	0.02	0.004	0.002	0.0006	0.0002	4.1	1.2	4.2	672	18300	460
11.25 to 12.0 μm	16	0.06	0.02	0.005	0.001	0.0007	0.0001	4.3	0.6	4.1	669	17700	400
12.0 to 12.75 μm	17	0.04	0.02	0.004	0.001	0.0007	0.0001	4.5	0.9	4.0	667	17400	366
12.75 to 13.5 μm	18	0.07	0.01	0.006	0.001	0.0006	0.0001	3.9	0.6	3.7	661	17100	324
13.5 to 14.25 μm	19	0.05	0.01	0.005	0.001	0.0007	0.0001	4.5	0.7	3.6	660	17000	300
14.25 to 15.0 μm	20	0.02	0.01	0.001	0.001	0.0005	0.0001	3.2	0.5	3.7	660	16800	280
Sample 0621a Depth profile 1													
Depth Interval	blk		1 s.e.		1 s.e.		1 s.e.		1 s.e.				
0.0 to 0.75 μm	1	0.11	0.04	0.005	0.002	0.0003	0.0001	2.2	0.5	2.2	622	18300	787
0.75 to 1.5 μm	2	0.08	0.02	0.004	0.002	0.0004	0.0001	2.6	0.4	2.0	616	18800	621
1.5 to 2.25 μm	3	0.04	0.02	0.002	0.001	0.0004	0.0001	2.6	0.7	2.3	623	18800	504
2.25 to 3.0 μm	4	0.05	0.00	0.009	0.002	0.0013	0.0004	8.5	2.4	3.3	653	18900	504
3.0 to 3.75 μm	5	0.04	0.01	0.016	0.004	0.0026	0.0003	16.5	2.0	4.0	668	17400	562
3.75 to 4.5 μm	6	0.05	0.01	0.024	0.005	0.0036	0.0006	23.5	3.6	3.8	663	16000	620
4.5 to 5.25 μm	7	0.05	0.01	0.033	0.007	0.0048	0.0008	31.0	5.1	3.4	654	15700	655
5.25 to 6.0 μm	8	0.05	0.01	0.041	0.008	0.0058	0.0009	37.3	5.8	3.4	654	16000	692
6.0 to 6.75 μm	9	0.05	0.01	0.043	0.008	0.006	0.001	40.5	6.1	3.1	649	15700	654
6.75 to 7.5 μm	10	0.04	0.01	0.039	0.008	0.007	0.001	45.2	6.8	3.0	645	16100	677
7.5 to 8.25 μm	11	0.046	0.003	0.05	0.01	0.008	0.002	50.8	11.4	2.9	643	15700	651
8.25 to 9.0 μm	12	0.050	0.003	0.06	0.01	0.009	0.002	54.7	12.4	2.9	642	15500	730
9.0 to 9.75 μm	13	0.051	0.003	0.06	0.01	0.009	0.002	55.8	12.6	3.1	648	15800	927
9.75 to 10.50 μm	14	0.045	0.003	0.06	0.01	0.010	0.002	61.7	14.4	3.3	652	15900	1090
10.5 to 11.25 μm	15	0.048	0.004	0.07	0.02	0.010	0.002	65.8	15.4	3.1	648	15700	1130
11.25 to 12.0 μm	16	0.047	0.002	0.070	0.009	0.011	0.001	69.6	8.6	2.9	643	15100	1150
12.0 to 12.75 μm	17	0.046	0.002	0.071	0.009	0.011	0.001	71.4	8.8	3.1	648	15800	1260
12.75 to 13.5 μm	18	0.046	0.002	0.07	0.01	0.012	0.001	74.6	9.4	3.0	646	15400	1250
13.5 to 14.25 μm	19	0.046	0.002	0.08	0.01	0.012	0.001	76.7	9.5	3.0	646	15400	1260
14.25 to 15.0 μm	20	0.047	0.004	0.08	0.01	0.012	0.001	74.4	9.3	3.2	649	15400	1230
Sample 0621a Depth profile 2													
Depth Interval	blk		1 s.e.		1 s.e.		1 s.e.		1 s.e.				
0.0 to 0.75 μm	1	0.08	0.02	0.006	0.001	0.0005	0.0001	3.4	0.5	2.7	638	17300	845
0.75 to 1.5 μm	2	0.05	0.01	0.015	0.007	0.0021	0.0009	13.8	5.9	4.1	670	18800	648
1.5 to 2.25 μm	3	0.052	0.002	0.066	0.008	0.009	0.001	59.7	7.8	4.7	681	14800	985
2.25 to 3.0 μm	4	0.045	0.004	0.08	0.01	0.012	0.001	79.3	8.5	3.7	661	13100	898
3.0 to 3.75 μm	5	0.044	0.003	0.09	0.01	0.015	0.002	94.3	9.9	3.0	645	12200	862
3.75 to 4.5 μm	6	0.050	0.003	0.12	0.02	0.017	0.003	108	16	2.8	640	11700	959
4.5 to 5.25 μm	7	0.046	0.002	0.12	0.02	0.019	0.003	123	19	2.8	640	11400	917
5.25 to 6.0 μm	8	0.051	0.004	0.14	0.02	0.020	0.003	130	20	3.0	646	11700	927
6.0 to 6.75 μm	9	0.048	0.003	0.13	0.02	0.020	0.003	127	18	2.8	640	11100	849
6.75 to 7.5 μm	10	0.048	0.005	0.13	0.02	0.020	0.003	129	18	2.8	640	11400	801
7.5 to 8.25 μm	11	0.047	0.002	0.15	0.03	0.022	0.005	142	30	2.7	636	11200	700
8.25 to 9.0 μm	12	0.049	0.004	0.15	0.03	0.022	0.004	138	28	2.6	635	11300	656
9.0 to 9.75 μm	13	0.052	0.003	0.16	0.03	0.022	0.004	142	28	2.7	637	11300	624
9.75 to 10.50 μm	14	0.053	0.005	0.15	0.03	0.021	0.004	133	25	2.6	635	11100	587
10.5 to 11.25 μm	15	0.051	0.003	0.15	0.03	0.021	0.004	137	25	2.6	635	11400	600
11.25 to 12.0 μm	16	0.053	0.002	0.18	0.02	0.025	0.003	159	18	2.7	637	11200	642
12.0 to 12.75 μm	17	0.045	0.003	0.15	0.02	0.025	0.003	159	19	2.8	639	11500	711
12.75 to 13.5 μm	18	0.047	0.002	0.16	0.02	0.025	0.003	159	19	2.9	641	11400	741

Table 4. (continued)

		$^{207}Pb^*/^{206}Pb^*$		$^{207}Pb^*/^{235}U$		$^{206}Pb^*/^{238}U$		$^{206}Pb/^{238}U$		Ti	Ti	Hf	Y
			+/-		+/-		+/-	Age (Ma)	+/-	ppm	°C	ppm	ppm
13.5 to 14.25 μm	19	0.046	0.003	0.17	0.02	0.026	0.003	166	20	2.8	640	11300	714
14.25 to 15.0 μm	20	0.052	0.003	0.19	0.02	0.026	0.003	167	20	3.0	644	11800	758

[a]Zircon crystallization temperatures are calculated using *Ferry and Watson* [2007]. The values reported in this table were used in the construction of the composite Figures 4–8. Refer article sections 3 and 4 for analytical details and data processing, including uncertainty calculations. Refer supporting information for additional data and data for the conventional spot-mode analyses.

concentration values from the depth profiles in Figures 6–8 correspond to 10% for Ti, 9% for Y, and 4% for Hf. This applied error is an estimate of the total error, which is computed by quadratic addition (rounded to the nearest integer) of the following 1σ uncertainties for each chemical species: (1) the uncertainty of Ti (8.8%), Y (1.4%), and Hf (0.43%) in the 91,500 standard [*Liu et al.*, 2010]; (2) The maximum observed depth variation of the Ti (4%), Y (8%), and Hf (4%) RSF factors; and (3) the average (n = 180) 1σ standard error of the mean (Ti = 3.3%, Y = 3.2%, and Hf = 1.4%) for individual five cycle groups of raw measurements from the unknowns.

4.1. PNG 03-118m

Zircons in sample PNG 03-118m exhibit a structure, as revealed by CL imaging of polished cross sections, consistent with young overgrowths on inherited cores and the U-Pb results confirm this interpretation. Spot-mode analyses of the interior portions of the polished zircon cross sections yield $^{206}Pb/^{238}U$ ages ranging from 49.9 ± 3.5 Ma (1σ) to 110 ± 5 Ma (1σ), with the bulk of analyses falling between 70 and 100 Ma (Figure 4a) whereas the spot-mode analyses on the unpolished zircon surfaces and the initial blocks of the depth profiles, yield ages <5 Myr.

Specifically, analytical blocks (e.g., Table 4) 1 through 15 of depth profile 1, blocks 1 through 11 of depth profile 2, blocks 1 through 6 of depth profile 3, and blocks 1 through 7 of depth profile 5, when treated as a single population, yield a model 1 age (Table 2) of 2.89 ± 0.29 Ma (MSWD = 2.2; Figure 5a). No regression is possible for the model 2 age. The model 3 and 4 ages (Table 2) for these analyses are 3.1 ± 1.3 Ma (MWSD = 0.93) and 1.1 ± 1.9 Ma (MSWD = 3.0), respectively. For the spot mode analyses made on polished cross sections and unpolished grain surfaces corresponding to calculated ages <5 Myr (Table 2), the model 1 through 4 (Table 2) ages are: 2.03 ± 0.34 Ma (MSWD = 6.5; Figure 5a), 1.56 ± 0.37 Ma (MSWD = 6.6; Figure 5a), 2.5 ± 2.4 Ma (MSWD = 3.6), and 1.9 ± 1.5 Ma (MSWD = 1.7). All of the zircon depth profiles for sample PNG 03-118m pass from the young overgrowths into an older zircon interior, the ages of which are consistent with the older spot-mode analyses from the polished zircon cross sections (Figure 4a and Table 4).

In order to assign a precise age for the young zircon overgrowths in this sample, it is necessary to consider that the analytical precision of the spot-mode analyses is greater due to longer counting time, whereas the lower spatial resolution may result in beam overlap onto older parts of the grain, potentially compromising accuracy. This is reflected in the high MSWD values for these analyses. The depth profiles are of lower analytical precision due to shorter counting time per depth interval, into which the profile was subdivided to achieve high spatial resolution. These factors result in a slight divergence between the different model ages for the depth profiles and <5 Myr spot-mode analyses. In this regard, the model 1 age of 2.89 ± 0.29 Ma for depth profile analyses is chosen as the best approximation of the crystallization age of the young zircon overgrowths because it is derived from data that only sampled the young zircon overgrowths (Figure 4a). This is the age that will be used in all future discussion of the young zircon overgrowths in this sample, but it is important to note that this age is very close to the ages determined using the other models, and thus our interpretation of this age, presented below, would not change by choosing a different model age for the young zircon overgrowths.

For depth profiles 1, 3, and 5, the concentration of Ti decreases steeply and steadily, starting at the unpolished zircon surface until the depth profile reaches the interface between the young overgrowth and the older core (Figure 6). In depth profile 2, the Ti concentration essentially remains unchanged throughout the young overgrowth. Zircon crystallization temperatures for the portions of the depth
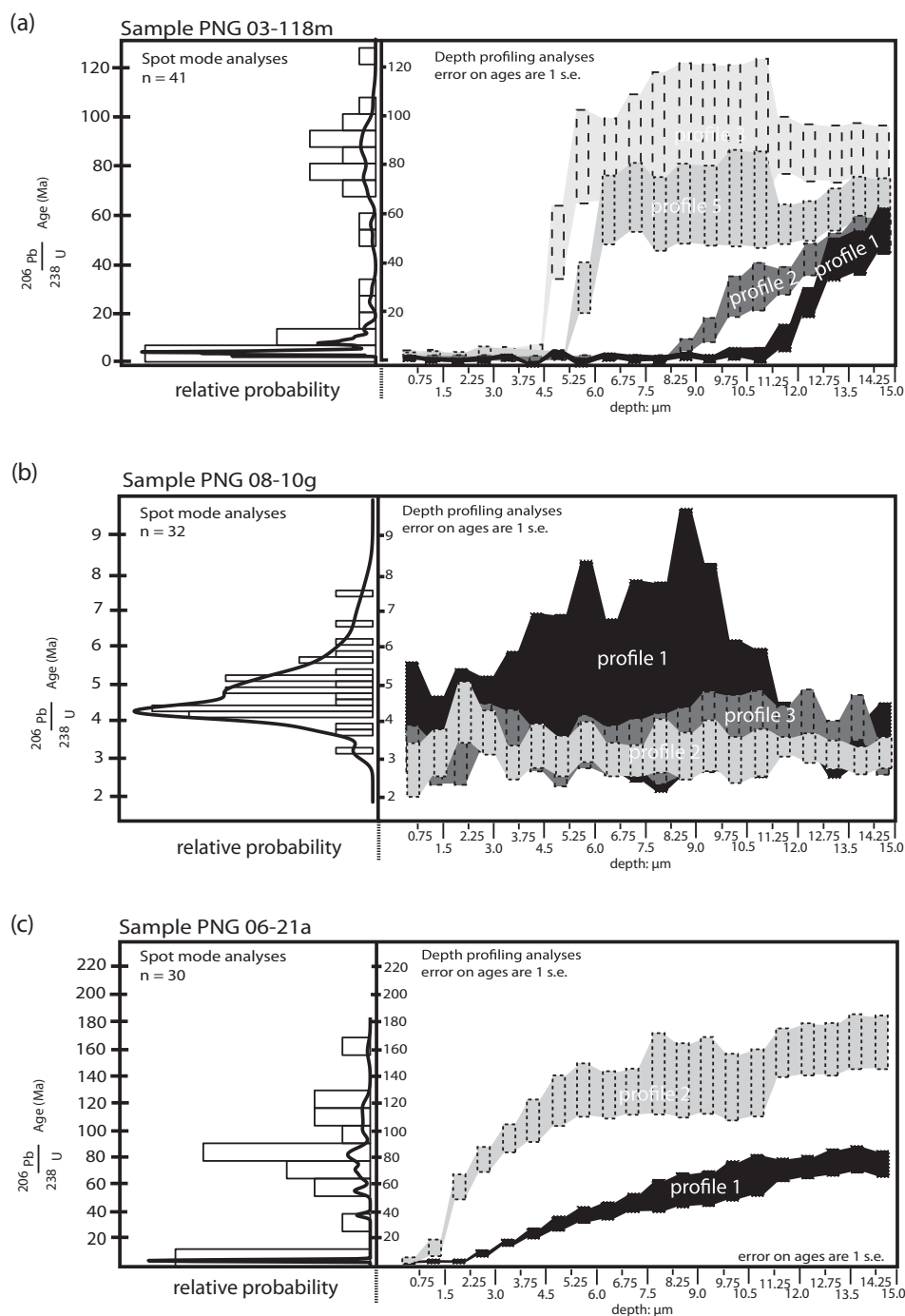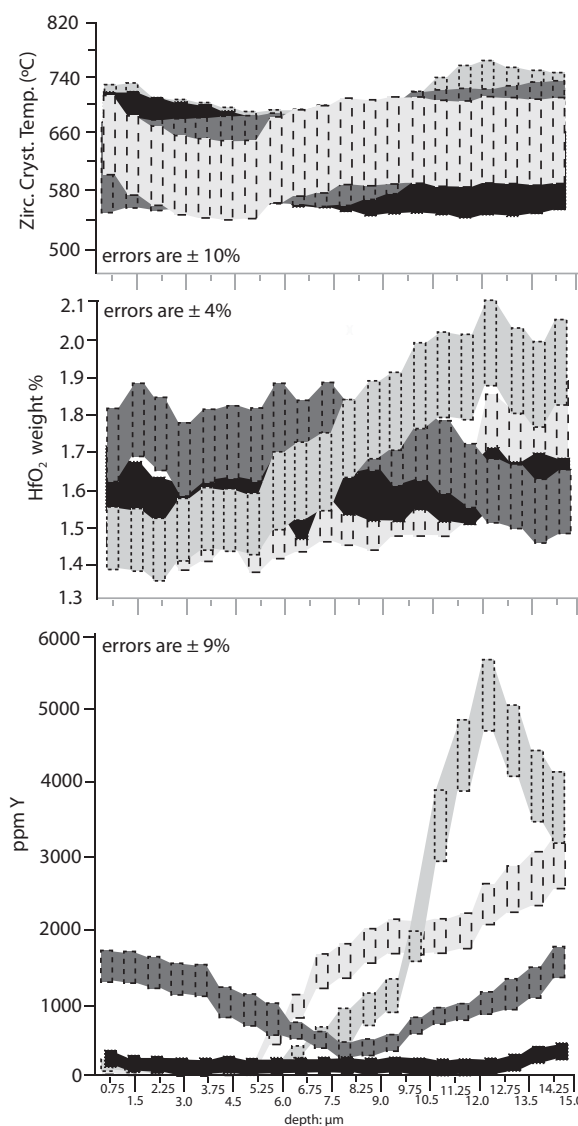
Figure 4. (**a**) U-Pb zircon results from sample PNG 03-118m. The depth profiles reveal both the age and thickness of the young overgrowths as well as the age of the inherited core. Refer to sections 3 and 4 for analytical details and data processing, including uncertainty calculations. (**b**)U-Pb zircon results from sample PNG 08-10g. Note the agreement between the [206]Pb/[238]U ages determined in spot and depth-profiling mode. There is no inherited zircon in this sample. Refer to sections 3 and 4 for analytical details and data processing, including uncertainty calculations. (**c**) U-Pb zircon results from sample PNG 06-21a. Zircons in this sample are characterized by thin overgrowths mantling an inherited core. Refer to sections 3 and 4 for analytical details and data processing, including uncertainty calculations.

profiles corresponding to the young zircon overgrowths, calculated using the observed Ti concentrations and assuming TiO$_2$ activity (a$_{TiO2}$) of one, vary between 665 ± 67°C and 590 ± 59°C, consistent with previously determined Ti in zircon temperature estimates on zircons in the mafic eclogite lens [*Monteleone et al.*, 2007].
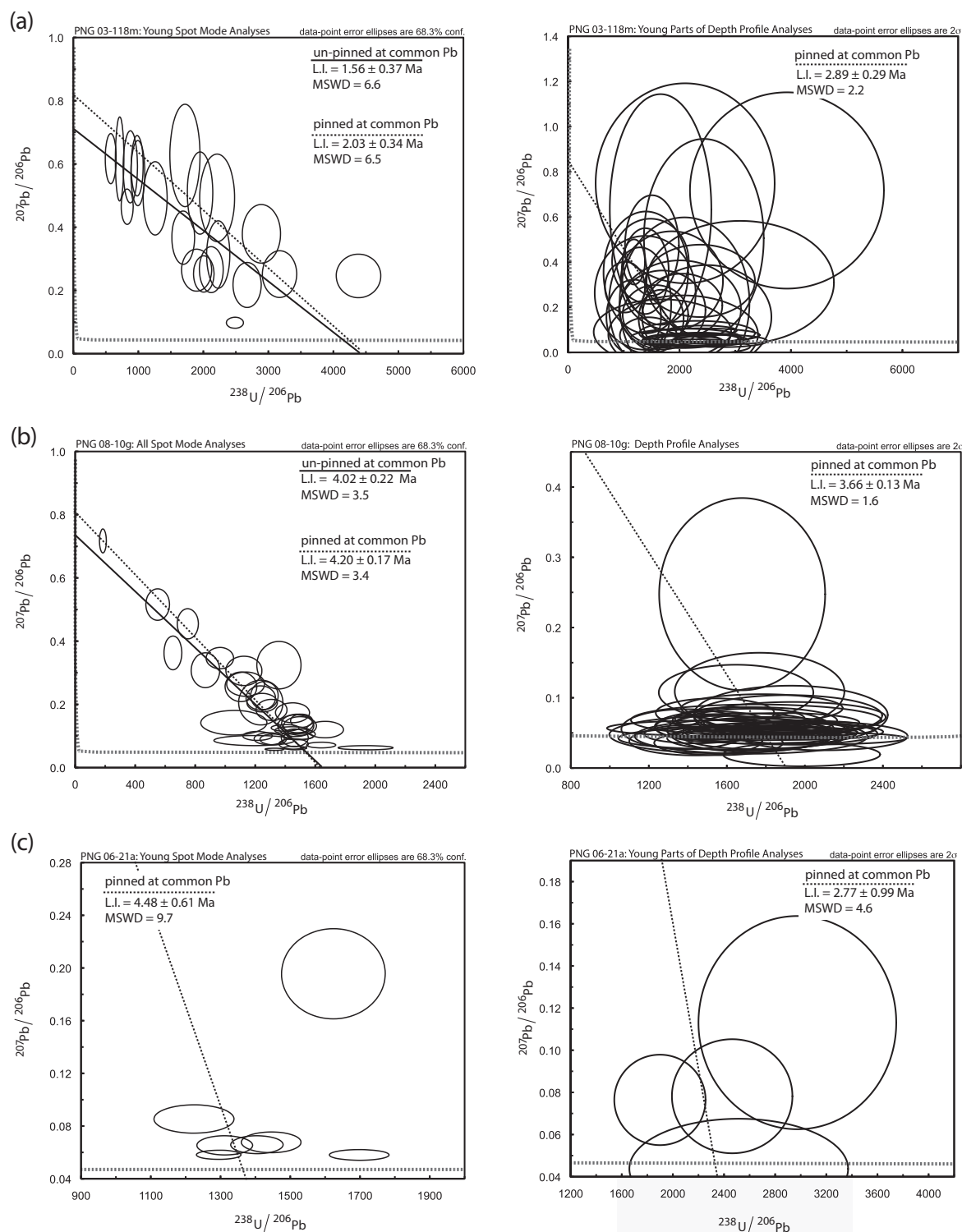
Figure 5. (**a**) Tera-Wasserburg diagrams for young (<5 Myr) spot analyses and young analytical blocks from the depth profiles for sample PNG 03-118m. (**b**) Tera-Wasserburg diagrams for all spot mode and depth profile analyses from sample PNG 08-10g. (**c**) Tera-Wasserburg diagrams for young spot-mode analyses and young analytical blocks from depth profiles for sample PNG 06-21a. Refer to results section for explanation of zircon populations used in these regressions.

Figure 6. Ti (shown here as zircon crystallization temperature, assuming crystallization pressure of 1 GPa and a_{SiO2} and a_{TiO2} of unity; see text for details), Hf, and Y results for depth profiles from sample PNG 03–118m. Refer to sections 3 and 4 for analytical details and data processing, including uncertainty calculations.

For depth profiles 1, 2, and 3, the concentration of Hf is invariant across the age boundary between the young overgrowth and the older core, whereas in profile 5, the concentration of Hf increases sharply for depths beyond the young overgrowth. Hf concentrations (reported as weight percent HfO_2) for the young overgrowths between ~1.8 wt % and 1.4 wt % are typical of zircon [e.g., *Hoskin and Schaltegger*, 2003].

In profiles 1, 3, and 5, the concentration of Y remains constant and is <200 ppm for all analyses occurring within the young zircon overgrowth. At the transition from young overgrowths to the older cores, the concentration of Y rises steeply for profiles 3 and 5, eventually attaining values >3000 ppm. In profile 2, the concentration of Y at the start of the depth profile is ~1500 ppm and then steadily declines over the region of the young overgrowth to ~500 ppm at the interface between the young overgrowth and the older interior. The concentration then steadily rises, but not as sharply as in profiles 3 and 5.

4.2. PNG 08-10g

Zircons in sample PNG 08-10g exhibit an oscillatory and complexly zoned structure, as revealed by CL imaging of polished cross sections. However, the combined spot-mode and depth-profiling results from this sample reveal a homogeneous age distribution both within individual zircons and across different zircons from this sample (Figure 4b). This sample illustrates that it is not possible to identify "inherited" zircon cores based on CL images alone. When all of the analytical blocks from the depth profiles are treated as a single population, the result is a model 1 age (Table 2) of 3.66 ± 0.13 Ma (MSWD = 1.6; Figure 5b) and a model 2 age (Table 2) of 2.3 ± 3.7 (MSWD = 1.6; Figure 5b). The model 3 and 4 ages (Table 2) are 3.60 ± 0.78 Ma (MSWD = 0.34) and 3.53 ± 0.80 Ma (MSWD = 0.38), respectively. When grouped together as a single population, all of the spot-mode analyses yield model 1 through 4 ages (Table 2) of: 4.20 ± 0.17 Ma (MSWD = 3.4; Figure 5b), 4.02 ± 0.22 Ma (MSWD = 3.5; Figure 5b), 4.6 ± 3.1 Ma (MSWD = 8.0), and 4.03 ± 0.94 Ma (MSWD = 0.6). The slightly older spot-mode ages in comparison to the depth profile ages likely reflect the intrinsically lower lateral resolution of the ion beam, resulting in beam overlap onto slightly older (but not inherited) interior domains. This is an important consideration in choosing an age that best reflects zircon crystallization in this sample. We use the model 1 age of 3.66 ± 0.13 Ma (Figure 5b) from the depth profile analyses for all future discussion of the time of zircon crystallization in this sample.
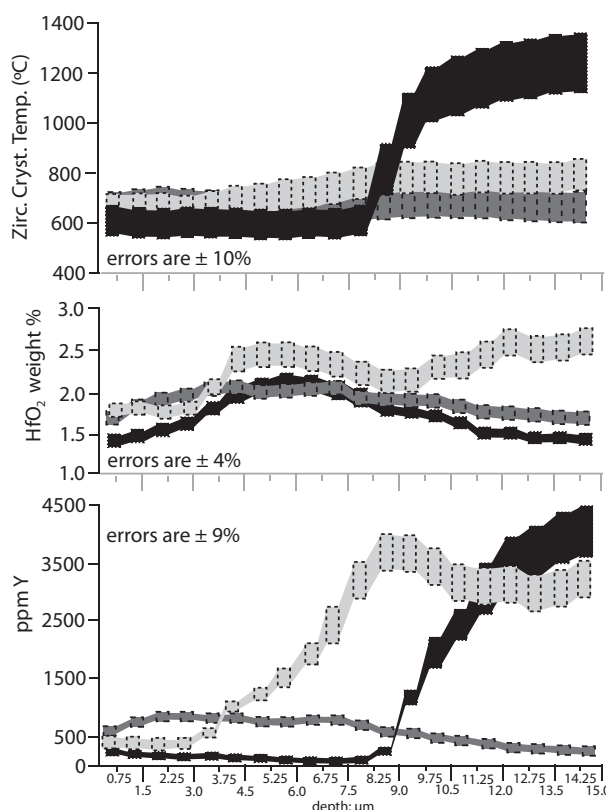
Figure 7. Ti (shown here as zircon crystallization temperature, assuming crystallization pressure of 1 GPa and a_{SiO2} and a_{TiO2} of unity; see text for details), Hf, and Y results for depth profiles from sample PNG 08–10g. Refer to sections 3 and 4 for analytical details and data processing, including uncertainty calculations.

Despite the homogeneous age population of zircons in this sample, Ti, Hf, and Y are heterogeneously distributed (Figure 7). Calculated zircon crystallization temperatures based on data from depth profiles 2 and 3 indicate temperatures between $650 \pm 65°C$ and $700 \pm 70°C$, whereas depth profile 1 exhibits a sharp increase from $600 \pm 60°C$ between the surface and a depth of 8.25 μm, up to an apparent temperature of $>1200 \pm 120°C$ between 8.25 and 15 μm (assuming $a_{TiO2} = 1$). An important note here, however, is that the intensity of ^{57}Fe begins to increase contemporaneously with Ti and Y in depth profile 1. This increase in ^{57}Fe is not observed in any other depth profiles, and could indicate that the ion beam passed into an inclusion within the zircon grain during this depth profile. The range in Hf concentrations throughout sample PNG 08-10g depth profiles is similar, but show heterogeneities throughout the individual profiles. Hf gradually increases during the first 3.75 μm of the profiles, roughly plateaus

between 3.75 and 7.50 μm, and then from 7.5 to 15 μm decreases steadily in profiles 1 and 3 but increases in profile 2. The concentration of Y is homogeneously distributed in depth profile 3, but not in profiles 1 and 2. The first 8.25 and 3.0 μm of profiles 1 and 2, respectively, exhibit a Y concentration similar to that of profile 3 (~450–600 ppm), however, the concentration of Y in profiles 1 and 2 then abruptly increases to levels above 3500 ppm.

4.3. PNG 06-21a

Zircons in sample PNG 06-21a exhibit structure, as revealed by CL imaging of polished cross sections, consistent with micron to submicron thick overgrowths on inherited cores and the U-Pb depth-profiling results confirm this interpretation. Spot-mode analyses of the interior portions of the polished zircon cross sections yield $^{206}Pb/^{238}U$ ages ranging from 3.8 ± 0.1 Ma to 1090 ± 52 Ma, with the bulk of analyses falling between ~60 and ~120 Ma (Figure 4c). For the purpose of comparison between the SIMS analyses in spot mode and the depth profiles from this sample, ages >220 Ma are excluded from Figure 4c, but data for all spot-mode analyses is provided in Table 3. The interior zircon ages reached in the depth profiles are broadly consistent with the older spot-mode analyses from the polished zircon cross sections (Figure 4c and Table 4).

Analytical blocks (e.g., Table 3) 1 through 3 of depth profile 1, and block 1 of depth profile 2, when treated as a single population, yield a model 1 age (Table 2) of 2.77 ± 0.99 Ma (MSWD = 4.6; Figure 5c), with no model 2 age possible. The model 3 and 4 ages (Table 2) are 2.7 ± 1.5 Ma (MSWD = 1.1) and 2.5 ± 3.0 Ma (MSWD = 4.6), respectively. Useful depth profile data are limited due to the thin young rims on the grains chosen for depth profiling, but the age calculations from the young parts of these four depth profiles correspond well to the <5 Ma spot-mode analyses made on the polished cross sections, which yield model 1, 3, and 4 ages (Table 2) of: 4.80 ± 0.61 Ma (MSWD = 9.1; Figure 5c), 4.4 ± 3.5 Ma (MSWD = 9), and 4.3 ± 2.3 Ma (MSWD = 2.9), respectively. No model 2 regression is possible for these analyses. As with the other samples
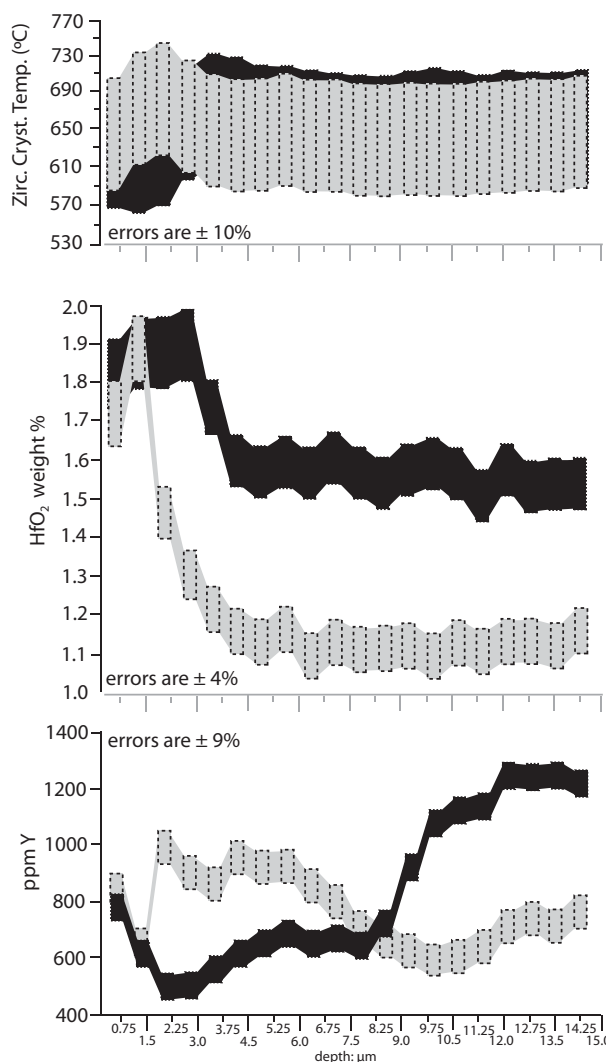
Figure 8. Ti (shown here as zircon crystallization temperature, assuming crystallization pressure of 1 GPa and a_{SiO2} and a_{TiO2} of unity; see text for details), Hf, and Y results for depth profiles from sample PNG 06–21a. Refer to sections 3 and 4 for analytical details and data processing, including uncertainty calculations.

in this study, spot analyses yield ages slightly older than those of the depth profiles, and we suspect beam overlap onto interior domains, and adopt the model 1 age from the depth profiles of 2.77 ± 0.99 Ma as the age of the zircon overgrowths in PNG 06-21a. This age is chosen because it has a lower MSWD value than most of the ages determined using the spot-mode analyses, and albeit based on a limited data set should best represent the age of the young overgrowths in this sample.

The calculated zircon crystallization temperatures for the first depth profile indicates temperatures of 620 ± 62°C for the first 2.25 μm of the profile, followed by an increase to a temperature of 670 ± 67°C at 3.0 μm, and then a decrease to 650 ± 65°C for the rest of the profile (Figure 8; assuming a_{TiO2} = 1). The first 0.75 μm of depth profile 2 yields a temperature of 640 ± 64°C. This is followed by an increase over the course of 1.5 μm to 680 ± 68°C. This rise is then followed by a decline to 650 ± 65°C for the remainder of profile 2.

The first 3.0 μm of depth profile 1 yielded Hf concentrations between 1.8 and 1.9 wt %, followed by a decrease to ∼1.6 wt % for the remainder of the profile. The first 0.75 μm of depth profile 2 has a Hf concentration of 1.7 wt %, followed by an increase to ∼1.9 wt % at 1.5 μm. Over the next 1.5 μm, the concentration of Hf measured in depth profile 2, steadily declines to ∼1.1 wt % where it remains until the end of the profile. The Y concentration in the first 1.5 μm are ∼800 and ∼600 ppm, respectively, for both depth profiles from PNG 06-21a. In depth profile 1, thereafter, the concentration of Y continues to decrease to ∼500 ppm corresponding to blocks three and four. This is followed by a gradual rise in Y (between 3.75 and 8.25 μm) reaching concentrations up to ∼600 ppm. At depths >8.25 μm the concentration of Y increases to values between 1100 and 1300 ppm for the remainder of profile 1. In depth profile 2, the concentration of Y increases after 1.5 μm to ∼1000 ppm. Thereafter, the concentration steadily decreases to a baseline concentration of ∼600 ppm at 9.75 μm. This is then followed by a gradual increase, eventually reaching ∼700 ppm, for the remainder of profile 2.

5. Interpretations and Discussion

The zircon SIMS analyses presented above are used to address three questions: (A) When did zircon in the quartzo-feldspathic host gneisses crystallize? (B) Are key trace elements (Y, Hf, and Ti) indicative of the

thermochemical environment during zircon crystallization? and (C) How do the spatial and temporal patterns of zircon crystallization in quartzo-feldspathic host gneisses relative to mafic eclogites from the Woodlark Rift compare with results from other (U)HP terranes?

Before answering these questions, it is first necessary to consider whether the data acquired in this study provides a sufficiently detailed spatial and age resolution to address these questions. In this regard, the depth profiles, despite being less numerous compared to the spot-mode SIMS analyses, are highly useful because they reveal U-Pb age and trace element variations at micron resolution starting at the unpolished exterior surface and penetrating up to and across the within-grain boundary between young overgrowth and inherited interiors. This advantage compensates for the relatively high U-Pb age uncertainties associated with many of the individual analytical blocks in the depth profiles. In fact, the conventional spot-mode analyses allow for a robust assessment of the U-Pb age relationships in these complex zircons, with the depth profile ages being complementary, and a guide for interpreting the Hf, Y, and Ti variations in unprecedented spatial detail.

5.1. When Did Zircon Crystallize in the Quartzo-Feldspathic Gneisses?

The results from sample PNG 08-10g allow for a comparison between the timing of zircon growth in quartzo-feldspathic host gneiss and the timing of zircon crystallization in coesite-eclogite formed at (U)HP conditions at ~7-8 Ma [*Monteleone et al.*, 2007; *Baldwin et al.*, 2008; *Zirakparvar et al.*, 2011]. The sample analyzed in this study is the host to partially retrogressed mafic-eclogite boudin that yielded LA-ICP-MS $^{206}Pb/^{238}U$ dates between 7.4 ± 1.1 and 4.1 ± 1.3 Ma for zircons from the unretrogressed portion of the eclogite, and 9.1 ± 0.6 to 3.8 ± 1.0 Ma for zircons extracted from the eclogite's retrogressed rind (sample PNG 08-10f of *Gordon et al.* [2012]). In comparing the 3.66 ± 0.13 Ma model 1 age for zircons in host gneiss PNG 08-10g with the previously published crystallization ages for zircons from these mafic eclogites as well as estimates of the timing of (U)HP metamorphism at this locality, zircon in the quartzo-feldspathic host gneiss crystallized subsequent to (U)HP metamorphism. Furthermore, a $^{40}Ar/^{39}Ar$ apparent age of 3.52 ± 0.10 Ma from a late-stage pegmatite dike (sample 89-320 in *Baldwin et al.* [1993]) at the coesite eclogite locality is within error of the model 1 zircon age in PNG 08-10g, suggesting zircon continued to crystallize during exhumation and may have been triggered by fluid infiltration. In the D'Entrecasteaux Islands, partial melting and synextensional magmatism occurred during rifting to exhume (U)HP rocks [e.g., *Hill et al.*, 1995; *Gordon et al.*, 2012]. The homogeneous zircon age population in PNG 08-10g may indicate it originated as a partial melt where preexisting zircons were completely dissolved during melting or were not present at all [e.g., *Miller et al.*, 2003; *Hongyan*, 2004]. This interpretation is further supported by CA-TIMS zircon $^{206}Pb/^{238}U$ zircon ages ranging from 3.49 ± 0.01 to 3.40 ± 0.02 Ma for a strongly deformed, 10 cm thick dike (sample PNG 08-10e) [*Gordon et al.*, 2012] that crosscuts the foliation in the host gneiss analyzed in this study (PNG 08-10g). However in contrast to the PNG 08-10g host gneiss, which showed no evidence of zircon inheritance, the discordant dike contains some inheritance [*Gordon et al.*, 2012]. In summary, when one considers all the available data at the coesite locality, evidence exists for zircon crystallization during peak (U)HP metamorphism in the coesite eclogite, and during subsequent exhumation in the host gneiss and crosscutting dikes, although not all bulk compositions preserve the complete history of zircon crystallization. Only zircons in the coesite eclogite constrain the timing of UHP metamorphism.

Zircons in samples PNG 06-21a and PNG 03-118m contain inherited cores with predominantly Cretaceous ages. This observation supports previous U-Pb analyses interpreted to indicate that the protoliths of quartzo-feldspathic high-grade and low-grade metamorphic rocks in the Woodlark Rift were part of a rift-related volcano-sedimentary system that formed during the development of the eastern Australian passive margin in the Late Cretaceous [*Zirakparvar et al.*, 2012].

Calculated U-Pb ages abruptly increase as the ion beam progressively samples from the young rim into the older interior domain of zircon as indicated by depth profile analyses of zircons from samples PNG 03-118m and PNG 06-21a. The number of analytical blocks corresponding to the limit between young rim and older interiors varies from grain to grain in samples PNG 03-118m and PNG 06-21a, but this is probably a function of mixing between the young overgrowth and the older core during ion beam sampling, rather than the existence of multiple age domains between the young overgrowth and old core in these grains. Such mixing during ion beam sampling is due to a combination of the inherent depth resolution of SIMS (knock-on effects in the primary ion collision cascade), the primary ion beam shape and secondary ion collection (e.g.,

heterogeneous beam density and incomplete exclusion of ions from crater edges), as well as mounting and crystallographic imperfections leading to oblique penetration of the depth profile across external and internal boundary surfaces. As such, zircons in samples PNG 03-118m and PNG 06-21a provide information about only two aspects of the Woodlark Rift: (a) the protoliths of some metamorphic rocks in the region as Late Cretaceous aged rift-related magmas and volcaniclastic sediments produced during the development of the eastern Australian passive margin [e.g., *Zirakparvar et al.*, 2012], and (b) the more recent history of rift-related exhumation as the Woodlark seafloor-spreading center rift tip propagated westward.

In terms of this more recent history, the model 1 age of 2.89 ± 0.29 Ma for the young zircon overgrowths in quartzo-feldspathic gneiss PNG 03-118m is close to within error of the 2.09 ± 0.49 Ma age determined by *Monteleone et al.* [2007] for zircon in a mafic eclogite that occurs as a lens within PNG 03-118m. The 2.09 ± 0.49 Ma age was interpreted as the time when the mafic eclogite crystallized at >14 kbar and 677 to 817°C, and it appears as though the metamorphic overgrowths in sample PNG 03-118m also formed around this time. This data supports the interpretation that a subduction complex has rifted apart to exhume eclogites ahead of the westward propagating seafloor-spreading rift tip [*Baldwin et al.*, 2012]. Also bearing on the more recent history of the Woodlark Rift is the age of 2.77 ± 0.99 Ma for the young zircon overgrowths in sample PNG 06-21a. This age predates the 1.4-1.5 Ma range of ^{40}Ar/^{39}Ar ages [*Baldwin et al.*, 1993] relating to the cooling history of the carapace shear zone, but significantly postdates the 68 ± 3.6 Ma garnet growth episode recorded by the Lu-Hf system <5 km away in the same shear zone [*Zirakparvar et al.*, 2011]. However, it is not possible to say more about the geodynamic context of zircon overgrowth formation in sample PNG 06-21a, except that it is likely that zircon growth occurred during exhumation. Such age heterogeneity is expected in subduction complexes.

In returning to the original question pertaining to the timing of zircon crystallization in the quartzo-feldspathic gneisses relative to the development of the Woodlark Rift, including (U)HP metamorphism, zircons from each of the samples examined appear to record different events. All zircons in quartzo-feldspathic gneiss sample PNG 08-10g crystallized subsequent to (U)HP metamorphism as recorded in the coesite eclogite. In sample PNG 06-21a, zircon overgrowths formed prior to mica crystallization within the Wakonai shear zone, but well after a poorly understood episode of garnet growth that forms porphyroclasts in the shear zone. This also suggests zircon overgrowth formation during processes associated with exhumation following peak metamorphism. Additionally, the age of zircon overgrowths in sample PNG 03-118m is only slightly older than the crystallization age of a mafic eclogite lens encapsulated by this sample, suggesting zircon overgrowth formation broadly contemporaneous with eclogite facies (HP) metamorphic conditions. In summary, zircon in quartzo-feldspathic host gneisses are documented to have grown during HP metamorphism and subsequent exhumation (i.e., over a wide range of P-T-t-D conditions), but do not record the timing of (U)HP metamorphism. It is necessary to examine the geochronologic record from all lithologies in a (U)HP terrane, since zircon in any one sample may not record the entire (U)HP metamorphic path- this is of particular importance in using this kind of data for determining exhumation rates.

5.2. Trace Element Behavior During Zircon Crystallization

The trace element (Hf, Y, and Ti) data collected during the depth-profiling analysis allows for an examination of the behavior of these elements during zircon rim formation in samples PNG 03-118m and PNG 06-21a, and zircon nucleation and growth in sample PNG 08-10g. In the case of the U-Pb analyses, we augmented the depth-profiling results with conventional spot-mode analyses to obtain a robust assessment of the U-Pb age variations in these zircons, but this is not necessary for the trace elements where data indicates trace element concentrations change throughout the zircon depth profiles at levels which are well beyond analytical error. It is these large magnitude changes that allow for an assessment of the behavior of these elements during zircon crystallization.

Trace element data from the depth profiles can be used to assess whether or not the individual zircons from a given sample were in geochemical equilibrium with each other at the time of crystallization. If individual samples were internally in equilibrium during zircon crystallization, it stands to reason that identical behavior of individual chemical species would be observed from grain to grain within a sample- excluding the inherited zircon cores in samples PNG 03-118m and PNG 06-21a. The concentration of an element will change, as progressive enrichment or depletion at the zircon-matrix interface would be expected to result in an increase or decrease in the concentration of the element during the interval of crystallization.

However, if zircons had attained chemical equilibrium during crystallization, one would predict the concentration changes of these trace elements to be the same from grain to grain.

In examining the trace element data within the context of the assumptions detailed above, it is clear that there is different behavior from grain to grain within each of the samples examined. To be certain that this variation reflects disequilibrium, though, diffusion must also be ruled out as a cause of the observed variations. This is especially relevant for samples PNG 03-118m and PNG 06-21a because they contain inherited cores, which would be expected to have a nonuniform trace element composition from grain to grain; these zircon cores could act as sinks or reservoirs of these elements by in-or-out diffusion during subsequent zircon overgrowth development. The fact that the depth profiles for samples PNG 03-118m and PNG 06-21a are characterized by abrupt changes (e.g., over the course of one or two 0.75 μm sized analytical blocks) in Ti, Hf, and Y concentrations corresponding to the location of the zircon age domain boundaries, strongly suggests that diffusion length scales across the boundary between young overgrowth and older cores are too small to be observable at the resolution of the SIMS depth profiles.

Diffusion, by its very nature, is a kinetic process seeking to attain chemical equilibrium, and as such significant diffusion would be expected to manifest itself in the depth profiles as a gradual concentration change across the sharp boundary between the young zircon overgrowth and older zircon core. This suggests that the effects of diffusive transfer across this boundary has not significantly contributed to the observed trace element characteristics in the young overgrowths, which is not an unexpected conclusion in light of previous studies showing that trivalent and tetravalent cation diffusion proceeds slowly in zircon over most geologic conditions [e.g., *Cherniak and Watson*, 2003]. Another important factor to rule out is the presence of inclusions as a contributing factor in the observed trace element compositions. In this regard, ^{57}Fe was monitored during depth profiling, and in the case of one depth profile (depth profile 1 for sample PNG 08-10g), there is a correlation between anomalously high Ti (and resultant temperature calculations) and the ^{57}Fe signal, this indicates part of this depth profile probably passed into an inclusion. This was the only profile, however, where the observed trace element variations could be correlated with changes in the ^{57}Fe signal.

Since diffusion and progressive matrix-grain boundary depletion or enrichment of Ti, Hf, and Y during zircon crystallization do not appear to be the cause of the observed grain to grain variation, and the contribution of these elements from inclusions can reasonably be ruled out for all but one of the depth profiles, this variation may instead reflect hand-sample-scale geochemical heterogeneity during zircon crystallization. This indicates that these samples were not in chemical equilibrium during zircon crystallization, which complicates the use of certain trace element species in assigning a set of P-T conditions to a U-Pb age. This interpretation supports prior investigations into the submicron-scale distributions of trace elements in zircons [e.g., *Hofmann et al.*, 2009], and limits the use of trace zircon trace element compositions to unambiguously tie zircon U-Pb ages to specific P-T conditions in samples where equilibrium was not achieved. This has implications for the use of zircon thermometry in (U)HP terranes as discussed below.

Thermometers based on the Ti content of zircon, which rely on equilibrium assumptions, have been widely applied to igneous and metamorphic rocks [*Ferry and Watson*, 2007; *Fu et al.*, 2008]. These thermometers are appealing because they can be used on individual zircons that have been removed from their host rock by artificial (e.g., laboratory separation of zircon) or natural (e.g., detrital zircons) means. These thermometers rely on thermodynamic models for the incorporation of Ti into zircon that have been calibrated in both experimental settings and in natural samples where the temperature of crystallization is already known [*Watson et al.*, 2006]. Since the degree to which Ti is incorporated into zircon depends on the activities of SiO_2 (a_{SiO_2}) and TiO_2 (a_{TiO_2}), temperature, and pressure, applications of Ti in zircon thermometers would be in situations where a_{SiO_2} and a_{TiO_2} and pressure constraints can be measured or constrained in conjunction with the concentration of Ti in zircon [*Ferry and Watson*, 2007; *Tailby et al.*, 2011], ideally where rutile and quartz coexist with zircon (e.g., as mineral inclusions). In the absence of such constraints for highly deformed (U)HP rocks, temperatures are necessarily model dependent, but we can nevertheless assess the degree of equilibration through a comparison between different crystals in individual samples.

Examination of the results of Ti thermometry calculations for the depth profiles from PNG 03-118m shows that for the case of three of the profiles, the calculated temperature decreases steadily and sharply from the grain surface to the interface between the overgrowth and the older core, whereas in one of the profiles,

the calculated temperature gradually increases over this interval. Temperature variations over the course of zircon rim formation is conceivable, but would not explain the divergent temperature-time paths between the three profiles that exhibit a decline in temperature versus the one profile that exhibits a temperature increase with crystal ages that decrease. Along the same line of reasoning, if all of the zircon grains within a sample exhibited similar Ti concentration gradients, the observation could be interpreted within the context of work by *Tailby et al.* [2011], who documents a substantial pressure effect on the solubility of Ti in zircon. Instead, this variation is probably due to the fact that the zircons extracted from this sample were probably not in equilibrium with each other during crystallization. To clarify, it is quite possible that the a_{SiO_2} and a_{TiO_2} applicable to the young overgrowth examined in depth profile 2 of sample PNG 03-118m (the one that exhibits an increase in temperature) are drastically different than those applicable to profiles 1, 3, and 5 (those exhibiting a decrease in temperature) of the same sample. It is also likely that a_{SiO_2} and a_{TiO_2} changed throughout the time period over which the overgrowths crystallized in this sample, but a lack of constraints on these parameters bars us from further quantifying temperature-time paths for zircon rim crystallization. This also holds for samples PNG 06-21a and PNG 08-10g, suggesting that the scale of geochemical hetero-geneity at the time of zircon crystallization is an important complicating parameter in applying Ti-in-zircon thermometry in (U)HP rocks. However, the data set suggests that zircon crystallization in these samples occurred generally at temperatures below 700 ± 70°C, in agreement with previous studies [*Monteleone et al.*, 2007; *Baldwin et al.*, 2008].

5.3. Comparison of the Temporal and Spatial Scales of Zircon Growth in the PNG Quartzo-Feldspathic Gneisses With Other (U)HP Terranes

It has been suggested that the (U)HP metamorphic terrane in the western Woodlark Rift of PNG is somewhat enigmatic in that, while it exhibits some of the characteristics of other large and small (U)HP terranes, it can-not be assigned to either category [e.g., *Gordon et al.*, 2012]. For example, the time scales and degree of par-tial melting associated with the transition from (U)HP metamorphism to exhumation in the Woodlark Rift are more akin to those in the world's small (U)HP metamorphic terranes, whereas many of these smaller terranes achieved peak metamorphic temperatures well beyond those observed in the PNG terrane, and also have been exhumed within the context of a convergent boundary as opposed to during rifting. Bearing on this issue is the fact that the metamorphic overgrowth texture observed in zircons from samples PNG 03-118m and PNG 06-21a are similar to ones documented in quartzo-feldspathic gneisses from some of the world's other (U)HP metamorphic terranes as discussed below. In cases where SIMS or sensitive high-resolution ion microprobe (SHRIMP) U-Pb ages are reported from such zircons, it is possible to compare them with the tim-ing of zircon growth in the PNG (U)HP terrane's quartzo-feldspathic gneisses.

In some (U)HP terranes, individual zircon grains in quartzo-feldspathic gneiss unambiguously exhibit multi-stage metamorphic overgrowth formation. For example, *Wan et al.* [2005] document zircons in granitic gneiss derived from the Dabie Orogen that are characterized by the presence of ~777 Ma inherited cores, coesite and omphacite-bearing 244 ± 5 Ma overgrowths, and thin 226 ±2 Ma mantles also containing min-eral inclusions reflecting formation at (U)HP conditions. In a separate study of zircons from granitoid gneiss from the Yinggelisayi (U)HP terrane in the Altyn Tagh [*Zhang et al.*, 2004], a similar structure to the zircons in the Dabie Orogen with three distinct zones (core, overgrowth, and mantle) was observed. In this exam-ple, where U-Pb ages of 809 ± 10 to 885 ± 21 Ma for inherited cores and 487 ± 10 Ma for metamorphic overgrowths are reported, the presence of (U)HP mineral inclusions in the overgrowths also allows the robust conclusion that the zircon overgrowths formed at (U)HP conditions. Unfortunately, the age of the outermost rim relative to (U)HP metamorphism and subsequent exhumation is less clear.

In contrast to the two examples provided above, there are also zircons in quartzo-feldspathic gneiss that record a protracted crystallization history related to (U)HP metamorphism, but not at the single grain level. For example, *Zhang et al.* [2008] report SHRIMP ages of 900 to 2500 Ma for inherited zircon cores and 450 to 425 Ma for zircon overgrowths in granulite facies gneisses from the north Quaidam (U)HP metamorphic terrane. In this example, the 450 to 425 Ma age range is interpreted as the duration of granulite facies meta-morphism accompanying the transition from high to medium pressure metamorphism during continental collision and subsequent exhumation. A similar result and interpretation is reported for zircons examined by *Leech et al.* [2007] from the Tso Morari (U)HP complex, where zircons extracted from quartzo-feldspathic gneisses are characterized by inherited cores spanning the Proterozoic and Paleozoic with metamorphic overgrowths ranging from 53.3 ± 0.7 to 45.2 ± 0.7 Ma. In this case, the range of ages for the overgrowths is

interpreted as reflecting ∼8 Myr of continuous zircon overgrowth crystallization beginning during (U)HP conditions and ending at amphibolite facies conditions, at which time the ^{40}Ar/^{39}Ar system also closed in the same rocks.

Returning to the PNG (U)HP terrane, the presence of inherited zircon cores in samples PNG 03-118m and PNG 06-21a is similar to the examples provided above. However, in contrast to the the Dabie and Yinggeli-sayi (U)HP terranes, none of the PNG zircons display a protracted crystallization history reflecting a progression of metamorphic conditions at the single grain level. Instead, the results from PNG are more similar to those in the Quaidam and Tso Morari (U)HP complexes, where zircon overgrowths are uniform in age at the single grain level, but yield a range of ages across the study area. Despite this similarity, there is still a major difference in the time scales of metamorphic zircon crystallization in PNG and all of the examples provided above. In the other (U)HP terranes, episodes of zircon growth during progressive metamorphism and exhumation are separated in time by between 8 and 25 Myr, whereas a significantly shorter age gap of <5 Myr can be resolved across all of the PNG samples.

The <5 Myr documented in the PNG (U)HP terrane for zircon growth during peak (U)HP conditions and subsequent exhumation, is similar to age variations in titanite [*Rubatto and Herman*, 2001] documented for (U)HP metamorphism and subsequent exhumation from the Dora Maira unit of the western Alps. Furthermore, zircons and monazites in white schist from the Dora Maira unit of the Western Alps (U)HP terrane, investigated via SIMS, are characterized by ∼265 Ma inherited cores mantled by up to four concentric zircon domains reflecting crystallization during a progression from prograde to peak (U)HP conditions at ∼34 Ma lasting only 1 to 2 Myr [*Gauthiez-Putallaz et al.*, 2013]. In this regard, direct comparison [e.g., *Malusa and Garzanti*, 2012; *Malusa et al.*, 2011] between the geodynamic settings of subduction and exhumation in the western Alps and those in the PNG (U)HP terrane are bolstered by geochronologic evidence for rapid transitions from prograde to peak to retrograde conditions [e.g., *Rubatto and Hermann*, 2003; *Rubatto et al.*, 2011; *Gauthiez-Putallaz et al.*, 2013] in the Western Alps.

6. Conclusions

Zircons extracted from three samples of quartzo-feldspathic gneiss in the western Woodlark Rift of PNG were investigated using multiple SIMS high spatial resolution analysis techniques in an attempt to characterize zircon growth relative to the documented history of (U)HP metamorphism and subsequent rock exhumation in the region. U-Pb ages were determined in spot and depth-profiling mode, along with Hf, Ti, and Y data during depth profiling. These observations allow for the following conclusions:

1. Zircons in two of the samples examined (PNG 03-118m and PNG 06-21a) are characterized by inherited cores with metamorphic overgrowths, whereas zircons in a third sample (PNG 08-10g) do not contain inheritance and are of uniform age. The inherited cores in samples PNG 03-118m and PNG 06-21a yield predominantly Cretaceous U-Pb ages which is consistent with the tectonic origin of these samples as part of the rifted eastern Australian margin [e.g., *Zirakparvar et al.*, 2012]. The 2.89 ± 0.29 Ma and 2.77 ± 0.99 Ma metamorphic overgrowths in samples PNG 03-118m and PNG 06-21a, respectively, are of uniform age and record crystallization during eclogite facies metamorphism and synextensional exhumation, respectively. The 3.66 ± 0.13 Ma age for zircon in sample PNG 08-10g postdates zircon growth in coesite eclogite but is synchronous with synextensional magmatism.

2. Contrasting Hf, Y, and Ti concentrations across correlative aged domains on different zircon grains within individual samples is an unexpected result. These contrasting trace element compositions are interpreted as reflecting hand-sample-scale geochemical heterogeneity during zircon crystallization and indicate chemical disequilibrium during zircon crystallization. Calculated temperatures of zircon crystallization are <700°C and consistent with previous zircon Ti thermometry estimates [e.g., *Baldwin et al.*, 2008].

3. Comparison of the SIMS zircon U-Pb results from quartzo-feldspathic gneisses in the PNG (U)HP metamorphic terrane with similar types of data from several other (U)HP terranes bolsters previous suggestions that the transition from peak metamorphic conditions to exhumation in the PNG (U)HP metamorphic terrane occurred more rapidly than in most other terranes. The rates of processes, and related zircon growth, in the PNG (U)HP terrane are more similar to the rates observed in the (U)HP terrane in the Western Alps. This is

important because it provides support for the use of the PNG (U)HP terrane as an active analogue for understanding the evolution of the Western Alps (U)HP terrane.

4. Because zircon crystallizes over a wide range of P-T conditions, detailed depth profiling may be required to accurately capture the timing and duration of zircon crystallization in quartzo-feldspathic host gneisses from (U)HP terranes.

References

Abers, G. A., A. Ferris, M. Craig, H. Davies, A. L. Lerner-Lam, J. C. Mutter, B. Taylor (2002), Mantle compensation of active metamorphic core complexes at Woodlark rift in Papua New Guinea, *Nature*, *418*, 862–864.

Aikman, A. B. (2007), *Tectonics of the Eastern Tethyan Himalaya*, PhD thesis, pp. 1–327, Aust. Natl. Univ., Canberra.

Baldwin, S. L., and T. R. Ireland (1995), A tale of two eras: Pliocene-Pleistocene unroofing of Cenozoic and late Archean zircons from active metamorphic core complexes, Solomon Sea, Papua New Guinea, *Geology*, *23*, 1023–1026.

Baldwin, S. L., G. S. Lister, E. J. Hill, D. A. Foster, and I. McDougall (1993), Thermochronologic constraints on the tectonic evolution of active metamorphic core complexes, D'Entrecasteaux Islands, Papua New Guinea, *Tectonics*, *1*, 611–628.

Baldwin, S. L., B. Monteleone, L. E. Webb P. G. Fitzgerald M. Grove, and E. J. Hill (2004), Pliocene eclogite exhumation at plate tectonic rates in eastern Papua New Guinea, *Nature*, *431*, 263–267.

Baldwin, S. L., L. E. Webb, and B. D. Monteleone (2008), Late Miocene coesite-eclogite exhumed in the Woodlark Rift, *Geology*, *36*, 735–738.

Baldwin, S. L., P. G. Fitzgerald, and L. E. Webb (2012), Tectonics of the New Guinea region, *Ann. Rev. Earth Planet. Sci.*, *40*, 495–520.

Black, L. P., et al. (2004), Improved $^{206}Pb/^{238}U$ microprobe geochronology by the monitoring of a trace-element-related matrix effect; SHRIMP, ID-TIMS, ELA-ICP-MS, and oxygen isotope documentation for a series of zircon standards, *Chem. Geol.*, *205*, 115–140.

Breeding, C. M., J. J. Ague, M. Grove, and A. Rupke (2004), Isotopic and chemical alteration of zircon by metamorphic fluids: U-Pb age depth-profiling of zircon crystals from Barrow's garnet zone, northeast Scotland, *Am. Mineral.*, *89*, 1067–1077.

Brownlee, S. J., B. R. Hacker, M. Salisbury, G. Seward, T. A. Little, S. L. Baldwin, and G. A. Abers (2011), Predicted velocity and density structure of the exhuming Papua New Guinea ultrahigh-pressure terrane, *J. Geophys. Res.*, *116*, B08206, doi:10.1029/2011JB008195.

Cherniak, D. J., and E. B. Watson (2003), Diffusion in zircon, *Rev. Mineral. Geochem.*, *53*, 113–143.

Davies, H. L. and R. G. Warren (1992), Eclogites of the D'Entrecasteaux Islands. *Contributions to Mineralogy and Petrology 112*, 463–474.

Davies, H. L. (2012), The geology of New Guinea: The cordilleran margin of the Australian continent, *Episodes*, *35*(1), 87–102.

Ferry, J. M., and E. B. Watson (2007), New thermodynamic models and revised calibrations for the Ti-in-zircon and Zr-in-rutile thermometers, *Contrib. Mineral. Petrol.*, *154*, 429–437.

Fu, B., F. Z. Page, A. J. Cavosie, J. Fournelle, N. T. Kita, J. S. Lackey, S. A. Wilde, and J. W. Valley (2008), Ti-in-zircon thermometry: Applications and limitations, *Contrib. Mineral. Petrol.*, *156*, 197–215.

Gao, X. Y., Y. F. Zheng, and Y. X. Chen (2011), U-Pb ages and trace elements in metamorphic zircon and titanite from UHP eclogite in the Dabie orogen: Constraints from P-T-t path, *J. Metamorph. Geol.*, *29*, 721–740.

Gauthiez-Putallaz, L., D. Rubatto, and J. Hermann (2013), Metasomatism in the Dora Maira whiteschists investigated by SHRIMP oxygen isotopes and U-Pb geochronology, *Mineral. Mag.*, *77*(5), 1148. [Available at http://goldschmidt.info/2013/abstracts/originalPDFs/2344.pdf.].

Gordon, S. M., M. Grove, D. L. Whitney, A. K. Schmitt, and C. Teyssier (2009a), Fluid-rock interaction in orogenic crust tracked by zircon depth profiling, *Geology*, *37*, 735–738.

Gordon, S. M., M. Grove, D. L. Whitney, A. K. Schmitt, and C. Teyssier (2009b), Time-temperature-fluid evolution of migmatite dome crystallization: Coupled U-Pbage, Ti thermometry, and O isotopic ion microprobe depth profiling of zircon and monazite, *Chem. Geol.*, *262*, 186–201.

Gordon, S. M., T. A. Little, B. R. Hacker, S. A. Bowring, M. Korchinski, S. L. Baldwin, and A. R. C. Kylander-Clark (2012), Multi-state exhumation of young UHP-HP rocks: Timescales of melt crystallization in the D'Entrecasteaux Islands, southeastern Papua New Guinea, *Earth Planet. Sci. Lett.*, *351*, 237–246.

Hanchar, J. M., and W. VanWestrenen (2007), Rare earth element behavior in zircon-melt systems, *Elements*, *3*, 37–42.

Harley, S. L., and N. M. Kelly (2007), Zircon: Tiny but timely, *Elements*, *3*, 13–18.

Harley, S. L., N. M. Kelly, and A. Moller (2007), Zircon behavior and the thermal histories of mountain chains, *Elements*, *3*, 25–30.

Hill, E. J., (1994), Geometry and kinematics of shear zones formed during continental extension in eastern Papua New Guinea, *J. Struct. Geol.*, *16*, 1093–1105.

Hill, E. J., S. L. Baldwin (1993), Exhumation of high-pressure metamorphic rocks during crustal extension in the D'Entrecasteaux region: Papua New Guinea. *J. Metam. Geol.*, *11*, 261–277.

Hill, E. J., S. L. Baldwin, and G. S. Lister (1995), Magmatism as an essential driving force for formation of active metamorphic core complexes in eastern Papua New Guinea, *J. Geophys. Res.*, *100*, 10,441–10,451.

Hofmann, A. E., J. W. Valley, E. B. Watson, A. J. Cavosie, and J. M. Eiler (2009), Sub-micron scale distributions of trace elements in zircon, *Contrib. Mineral. Petrol.*, *158*, 317–335.

Hongyan, L. (2004), SHRIMP dating and recrystallization of metamorphic zircons from a granitic gneiss in the Sulu UHP terrane, *J. Geol. Soc. China*, *78*, 146–154.

Hoskin, P. W. O., and U. Schaltegger (2003), The composition of zircon and igneous and metamorphic processes, in *Zircon*, edited by J. M. Hancahr and P. W. O. Hoskin, *Rev. Mineral. Geochem.*, *5*, 27–62.

Ireland, T. R., and I. S. Williams (2003), Considerations in zircon geochronology by SIMS, *Rev. Mineral. Geochem.*, *53*, 215–241.

Leech, M., S. Singh, and A. K. Jain (2007), Continuous metamorphic zircon growth and interpretation of U-Pb SHRIMP dating: An example from the western Himalaya, *Int. Geol. Rev.*, *49*, 313–328.

Liati, A. (2005), Identification of repeated Alpine (ultra) high-pressure metamorphic events by U-Pb SHRIMP geochronology and REE geochemistry of zircon: The Rhohdope zone of Northern Greece, *Contrib. Mineral. Petrol.*, *150*, 608–630.

Little, T. A., S. L. Baldwin, P. G. Fitzgerald, and B. D. Monteleone (2007), Continental rifting and metamorphic core complex formation ahead of the Woodlark spreading ridge, D'Entrecasteaux Islands, Papua New Guinea, *Tectonics*, *26*, TC1002, doi:10.1029/2005TC001911.

Little, T. A., B. R. Hacker, S. M. Gordon, S. L. Baldwin, P. G. Fitzgerald, S. Ellis, and M. Korchinski (2011), Diapiric exhumation of Earth's youngest (U)HPeclogites in the gneiss domes of the D'Entrecasteaux Islands, Papua New Guinea, *Tectonophysics*, *510*, 39–68.

Liu, Y. S., Z. C. Hu, K. Q. Zong, C. G. Gao, S. Gao, J. Xu, and H. H. Chen (2010), Reappraisement and refinement of zircon U-Pb isotope and trace element analyses by LA-ICP-MS, *Chin. Sci. Bull.*, *55*, 1535–1546.

Lus, W. Y., I. McDougall, and D. L. Hug (2004), Age of metamorphic sole of Papuan Ultramafic Belt ophiolite, Papua New Guinea, *Tectonophysics*, *392*, 85–101.

Malusa, M. G., and E. Garzanti (2012), Actualistic snapshot of the early Oligocene Alps: The Alps-Apennines knot disentangled, *Terra Nova*, *24*, 1–6.

Malusa, M. G., C. Faccenna, E. Garzanti, and R. Polino (2011), Divergence in subduction zones and exhumation of high pressure rocks (Eocence Western Alps), *Earth Planet. Sci. Lett.*, *310*, 21–32.

Martinez, F., A. Goodliffe, and B. Taylor (2001), Metamorphic core complex formation by density inversion and lower crustal extension, *Nature*, *411*, 930–933.

McClelland, W. C., and T. J. Lapen (2013), Linking time to the pressure-temperature path for ultra-high pressure rocks, *Elements*, *9*(4), 273–280.

McClelland, W. C., J. A. Gilotti, F. K. Mazdab, and J. L. Wooden (2009), Trace-element record in zircons during exhumation from UHP conditions, North-East Greenland Caledonides, *Eur. J. Mineral.*, *21*, 1135–1148.

Miller, C. F., S. M. McDowell, and R. W. Mapes (2003), Hot and cold granites? Implications of zircon saturation temperatures and preservation of inheritance, *Geology*, *31*, 529–532.

Miller, S. R., S. L. Baldwin, and P. G. Fitzgerald (2012), Transient fluvial incision and active surface uplift in the Woodlark Rift of eastern Papua New Guinea, *Lithosphere*, *4*(2), 131–149, doi:10.1130/L135.1.

Monteleone, B. D., S. L. Baldwin, T. R. Ireland, and P. G. Fitzgerald (2001), Thermochronologic constraints for the tectonic evolution of the Moresby Seamount, Woodlark Basin, Papua New Guinea, in Proceedings of the Ocean Drilling Program, edited by P. Huchon, B. Taylor, and A. Klaus, Sci. Results, 180, 1–35.

Monteleone, B. D., S. L. Baldwin, L. E. Webb, P. G. Fitzgerald, M. Grove, and A. K. Schmitt (2007), Late Miocene-Pliocene eclogite facies metamorphism, D'Entrecasteaux Islands, SE Papua New Guinea, *J. Metamorph. Geol.*, *25*, 245–265.

Paces, J. B., J. D. Miller (1993), Precise UôPb ages of Duluth Complex and related mafic intrusions, north-eastern Minnesota: geochronological insights to physical, petrogenetic, paleomagnetic, and tectonomagmatic processes associated with the 1.1 Ga midcontinental rift system. *Journal of Geophysical Research*, *98*, 13997–14013.

Rubatto, D., (2002), Zircon trace element geochemistry: Portioning with garnet and the link between U-Pb ages and metamorphism, *Chem. Geol.*, *184*, 123–138.

Rubatto, D., and J. Hermann (2001), Exhumation as fast as subduction?, *Geology*, *29*(1), 3–6.

Rubatto, D., and J. Hermann (2003), Zircon formation during fluid circulation in eclogites (Monviso, Western Alps): Implications for Zr and Hf budget in subduction zones, *Geochim. Cosmochim. Acta*, *67*, 2173–2187.

Rubatto, D., and J. Hermann (2007), Zircon behavior in deeply subducted rocks, *Elements*, *3*, 31–35.

Rubatto, D., D. Gebauer, and M. Fanning, (1998), Jurassic formation and Eocene subduction of the Zermatt-Saas-Fee ophiolites: Implications for the geodynamic evolution of the Central and Western Alps, *Contrib. Mineral. Petrol.*, *132*, 269–287.

Rubatto, D., D. Regis, J. Hermann, K. Boston, M. Engi, M. Beltrando, and S. R. B. McAlpine (2011), Yo-yo subduction recorded by accessory minerals in the Italian Western Alps, *Nat. Geosci.*, *4*, 338–342, doi:10.1038/NGEO1124.

Sanudo-Wilhemy, S. A., and A. R. Flegal (1994), Temporal variations in lead concentrations and isotopic compositions in the Southern California Bight, *Geochim. Cosmochim. Acta*, *67*, 3315–3320.

Scherer, E. E., M. J. Whitehouse, and C. Munker (2007), Zircon as a monitor of crustal growth, *Elements*, *3*, 19–24.

Schmitt, A. K., M. Grove, M. T. Harrison, O. Lovera, J. Hulen, and M. Walters (2003), The Geysers–Cobb mountain magma system, California (part 1): U-Pb zircon ages of volcanic rocks, conditions of zircon crystallization and magma residence times, *Geochim. Cosmochim. Acta*, *67*, 3423–3442.

Schneider, D. A., C. Senkowski, H. Vogel, G. Grasemann, C. H. Iglseder, and A. K. Schmitt (2011), Eocene tectonometamorphism on Serifos (western Cyclades) deduced from zircon depth-profiling geochronology and mica thermochronology, *Lithos*, *125*(1–2), 151–172, doi:10.1016/j.lithos.2011.02.005.

Tailby, N. D., et al. (2011), Ti site occupancy in zircon, *Geochim. Cosmochim. Acta*, *75*, 905–921.

Taylor, B., A. Goodliffe, F. Martinez, and R. Hey (1995), Continental rifting and initial seafloor spreading in the Woodlark Basin, *Nature*, *374*, 534–537.

Trail, D., S. J. Mojzsis, and T. M. Harrison (2007), Thermal events documented in Hadean zircons by ion microprobe depth profiles, *Geochim. Cosmochim. Acta*, *71*, 4044–5065.

Wan, Y., R. Li, S. A. Wilde, D. Liu, Z. Chen, L. Yan, T. Song, and X. Yin, (2005), UHP metamorphism and exhumation of the Dabie Orogen, China: Evidence from SHRIMP dating of zircon and monazite from a UHP granitic gneiss cobble from the Hefei Basin, *Geochim. Cosmochim. Acta*, *69*, 4333–4348.

Watson, E. B., D. A. Wark, and J. B. Thomas (2006), Crystallization thermometers for zircon and rutile, *Contrib. Mineral. Petrol.*, *151*, 413–433.

Webb, L. E., S. L. Baldwin, T. A. Little, P. G. Fitzgerald (2008), Can microplate rotation drive subduction inversion?, *Geology*, *36*, 823–826.

Zirakparvar, N. A., S. L. Baldwin, and J. D. Vervoort (2011), Lu-Hf garnet geochronology applied to plate boundary zones: Insights from the (U)HP terrane exhumed within the Woodlark Rift, *Earth Planet. Sci. Lett.*, *309*, 56–66.

Zirakparvar, N. A., S. L. Baldwin, and J. D. Vervoort (2012), The origin and geochemical evolution of the Woodlark Rift of Papua New Guinea, *Gondwana Res.*, *23*(3), 931–943, doi:10.1016/j.gr.2012.06.013.

Zhang, A., L. Liu, Y. Sun, D. Chen, Y. Wang, and J. Luo (2004), SHRIMP U-Pb zircon ages for the UHP metamorphosed granitoid gneiss in the Altyn Tagh and their geological significance, *Chin. Sci. Bull.*, *49*, 2527–2532.

Zhang, J., C. G. Mattinson, F. Meng, Y. Wan, and K. Tung (2008), Polyphase tectonothermal history recorded in granulitized gneisses from the north Quaidam HP/UHP metamorphic terrane, western China: Evidence from zircon U-Pb geochronology, *GSA Bull.*, *120*, 732–749.

Zou, H., Q. Fan, A. K. Shmitt, and J. Sui (2010), U-Th dating of zircons from Holocene potassic andesites (Maanshan volcano, Tengchon, SE Tibetan Plateau) by depth profiling: Time scales and nature of magma storage, *Lithos*, *118*, 202–210.